Tristan Cren, Christophe Brun, and Dimitri Roditchev

3 STM studies of vortex cores in strongly confined nanoscale superconductors

Abstract: Vortices in superconductors are defined by two characteristic length scales, the penetration depth and the coherence length. In this chapter, we address the case where the penetration depth is much larger than the size of the superconducting samples and for which there is almost no screening of the magnetic field. In this limit, the image of vortices as bundles of flux is no longer correct and the confinement effects are governed by the coherence length, which corresponds to the size of the vortex core in which the order parameter vanishes. We thus address the problem of the vortex phases in strongly confined superconductors where the lateral size is a few times the coherence length. The natural probe at this scale is scanning tunneling microscopy/spectroscopy which have allowed us – since the pioneering work of Hess et al. – to visualize both the vortex core and the supercurrent density at the nanometer scale. Using a combined experimental and theoretical approach we show that the vortex phases are governed by the competition between the loss of condensation energy in the vortex core and the kinetic energy of the vortex and Meissner currents. In a first part we describe some extreme confinement effects observed recently in nanoscale two-dimensional superconductors. We start with the case of a system so small that it can only accept a single vortex. Then we discuss some recent scanning tunneling spectroscopy experiments that revealed novel ultradense arrangements of single Abrikosov vortices characterized by an intervortex distance up to 3 times shorter than the bulk critical one. At yet stronger confinement, we show that giant vortices, corresponding to the merging of several vortices into a single one, are indeed observed and their structure is discussed. In a second part, we demonstrate that vortices also exist inside Josephson junctions formed by two neighboring superconductors coupled by a metallic link. We discuss the analogy and difference between the recently observed Josephson proximity vortices and the usual Abrikosov vortices.

3.1 Introduction: Vortices in strongly confined superconductors

Confinement effects occur as soon as one of the dimensions of a superconducting sample becomes comparable to one of its characteristic length scales, ξ and λ. The purpose of this chapter is to explore the vortex confinement in superconducting islands

Tristan Cren, Christophe Brun, Institut des NanoSciences de Paris, CNRS & Sorbonne Universités (UPMC), Paris, France
Dimitri Roditchev, Laboratoire de Physique et d'Etude des Matériaux, ESPCI Paris, PSL Research University, CNRS

DOI 10.1515/9783110456806-004,

with lateral dimension D comparable to the coherence length, $\xi \sim D$, for which the magnetic penetration depth is much greater than the lateral dimension $\lambda \gg D$. In this limit, we will show that the well-forged image of vortices as magnetic flux tubes is totally irrelevant. Paradoxically, this makes the understanding of confinement phenomena easier because we can completely neglect the spatial variation of the magnetic field induced by the circulation of supercurrents. To understand the limits that we will explore one must first recall some basic notions of bulk superconductors using the Ginzburg–Landau approach [25]. We will show how low dimensionality, in thickness or in lateral dimension, induces new behaviors that are difficult to grasp with the bulk superconductor concepts. Once equipped with the right tools, we will address some issues that naturally come to mind when one looks at the confined vortices: what will happen when the size of a superconductor becomes comparable or even smaller than one (or two!) of its characteristic lengths? Which properties of bulk superconductors remain in strong confinement regime? Which new phenomena appear? Heading towards the nanoscale we will witness the emergence of new behaviors.

In this chapter, we will describe the mechanisms at work for vortex interaction and confinement phenomena in nanosystems. The most important message we intend to convey is that nanosuperconductors are within a limit where minimizing the kinetic energy of the currents in the system plays a fundamental role in the organization of vortices. In particular, the competition between the Meissner currents, generated by the magnetic field, and the vortex currents results in oscillatory behaviors that bear some similarities with the Little–Parks effect of the critical temperature as a function of the magnetic field in superconducting rings [38]. In 1965, D. Saint James [51] calculated that the critical field of a superconducting cylinder should be strongly modulated as a function of its diameter when it reaches dimensions comparable with a few ξ. In the same vein, in 1966 Fink & Presson [22, 23] calculated that the free energy of a nanocylinder should be modulated by the magnetic field due to partial compensation between Meissner currents and vortex currents. More recently, the exploration of Ginzburg–Landau equations in different geometries motivated by experimental work on mesoscopic superconductors [10, 24, 39] showed that particular vortex configurations, that do not exist in volume, could be favored by size or geometry effects [8, 20, 53]. For instance, confinement could in principle stabilize some fivefold vortex configurations which in principle cannot exist in bulk superconductors (Figure 3.1a). More surprisingly, it was predicted that stable vortex-antivortex configurations could be stabilized in some triangular-shaped samples [13]. This prediction was recently confirmed by Bogoliubov-de Gennes calculations for square shaped samples [63]. Finally, one of the main challenges in the study of vortex confinement came from the prediction of the existence of giant vortices [8, 20, 22, 23, 40, 52, 53]. Numerical simulations predicted that, in the extreme confinement regime, several vortices could merge, forming giant vortices characterized by a 4π, 6π, 8π … winding of the phase instead of 2π for Abrikosov vortices (Figure 3.1b).

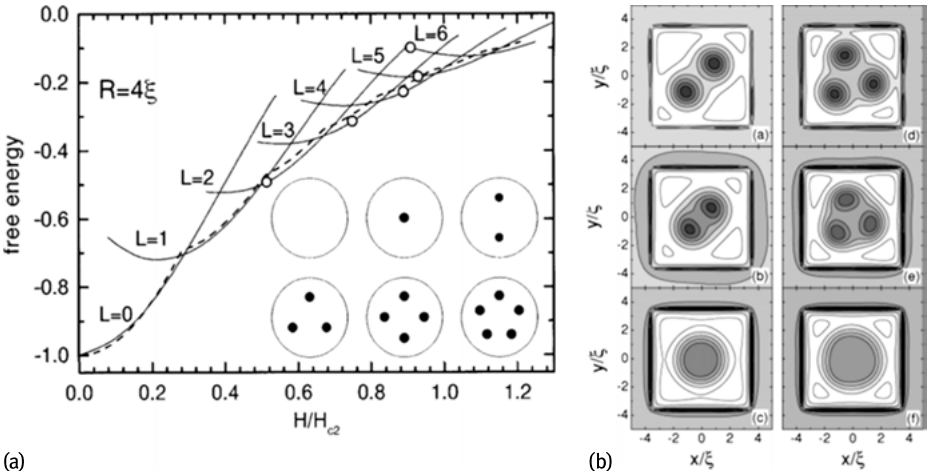

Fig. 3.1: (a) Ginzburg–Landau simulation of vortex confinement in disks of radius $R = 4\xi$ [53]. A pentagonal configuration is stabilized, while in volume such a configuration is excluded. (b) Ginzburg–Landau calculations of the magnetic field distribution for a square sample [8]. Depending on the field the system is in a configuration with a vorticity $L = 2$ for $H/H_{c2} = 0.42$ (a), $H/H_{c2} = 0.52$ (b), and $H/H_{c2} = 0.62$ (c). The system is in a configuration with a vorticity $L = 3$ for $H/H_{c2} = 0.62$ (d), $H/H_{c2} = 0.72$ (e), $H/H_{c2} = 0.82$ (f). For a given vorticity the system changes from a multivortex to a giant vortex configuration. Between (a) and (b) and between (d) and (e) one can observe how the vortices move closer to each other under the effect of the pressure of the Meissner currents when the field increases.

In addition to vortices in superconductors, one might also look for vortices in normal metals! As strange as it seems, proximity Josephson vortices living in the normal part of superconducting-normal-superconducting junctions (S–N–S) were recently predicted by Cuevas & Bergeret [9, 17]. The existence of Josephson vortices has been proposed since the 1960s to explain the critical current modulations of large Josephson junctions in a magnetic field [14, 61], but these vortices were supposed to have no core, at least in the S–I–S Josephson junction. Bergeret & Cuevas predicted that in fact in large S–N–S junctions, Josephson vortices could be very similar to Abrikosov vortices with a normal core surrounded by a minigap. This new type of object could be of great interest for the realization of highly integrated quantum electronics devices. Indeed, if instead of normal metals one exploited topological insulator surface states for the normal link of S–N–S junctions, then proximity vortices could exhibit Majorana bound states which are key ingredients for quantum computing.

In this chapter, we will explore a wide range of vortex confinement starting from the extreme case of an island that can accept only one vortex in which the effects of a supercurrent on the phase diagram are obvious. Then we will address the case of slightly larger systems that can accept several vortices but where strong confinement effects are still present. We will show that under certain strong confinement condi-

tions several vortices can be pushed to merge so as to form giant vortex states. Then we will describe some recent experiments on the generation of proximity vortices in nanoscale S–N–S Josephson junctions.

3.2 Theoretical approach of vortices confined in systems much smaller than the penetration depth

3.2.1 Characteristic length scales

In samples with characteristic dimensions D much smaller than the London penetration depth $D \ll \lambda_L$ (see Figure 3.2) the magnetic field almost completely penetrates the sample and is substantially equal to the applied field in the absence of the sample. To get an idea of the orders of magnitude, consider a thin plate of thickness a placed in a magnetic field $\mu_0 \boldsymbol{H}_0$ parallel to the surface of the plate. When the thickness of the plate is much smaller than the penetration depth, $a \ll \lambda_L$, the expression of the field at the center is $\boldsymbol{B}(z=0) \approx \mu_0 \boldsymbol{H}_0 \left[1 - (a/2\lambda_L)^2\right]$. Thus, for a thin plate with $a = 0.1\lambda_L$, the magnetic field in the center is $\boldsymbol{B} = 0.9975\mu_0 \boldsymbol{H}_0$, i.e., only 0.25% less than the applied field. In the following, we will therefore overlook the field induced by the currents flowing in the samples and only consider the applied field (see Figure 3.2). Another major consequence is that the energy of expulsion of the magnetic field, which usually plays a very important role in bulk superconductors, can be totally neglected, which will make the understanding of the phenomena easier. However, this limit is quite frequently a source of misunderstanding for those accustomed with intuitive images forged from the bulk case. Therefore, we will briefly present below a theoretical development for the changes that are seen with this limit in comparison to the usual case where the magnetic response generally cannot be overlooked.

In addition to the penetration depth, a second length scale plays a fundamental role in superconductors; this is of course the coherence length, ξ. In Ginzburg–Landau theory it is expressed as $\xi_{\mathrm{GL}} = \sqrt{\frac{\hbar^2}{8m|\alpha|}}$. In Bardeen–Cooper–Schrieffer (BCS) theory that length takes a more intuitive form given by $\xi_{BCS} = \hbar v_{\mathrm{F}}/\pi\Delta$. This coherence length defines the characteristic length scale over which the order parameter can vary. For instance, the order parameter, which vanishes in the vortex center, is restored over a typical distance ξ of its core.

The characteristic lengths λ and ξ are not intangible constants of materials but depend on both temperature and disorder. The disorder decreases the effective value of ξ but increases that of λ, so that any type I superconductor becomes type II when the mean free path of electrons is sufficiently affected by the disorder. In the diffusive

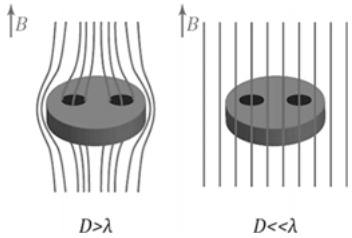

Fig. 3.2: Schematic picture highlighting the difference between a superconducting disk with diameter $D > \lambda$ in which the magnetic field is screened on the edge by Meissner currents and in which Abrikosov vortices behaves like flux bundles. The flux lines in blue show that the magnetic field is strongly affected by the response of the sample. In the opposite limit, for samples much smaller than the penetration depth $D \ll \lambda$, the flux lines are not affected by the response of the sample that is completely negligible, and the magnetic field is practically equal to the applied magnetic field. In this limit, the vortices can no longer be considered to be flux bundles.

limit, that is to say when $l \ll \xi_0$, the effective lengths are given by [19]:

$$\xi(T, l) \approx 0.85\sqrt{l\xi_0(T)}$$

$$\lambda(T, l) \approx 0.64\lambda_0\sqrt{\frac{\xi_0(T)}{l}}$$

Where ξ_0 and λ_0 are the coherence and penetration length in the absence of disorder. Note that even in the absence of disorder, type I superconductors become type II in sufficiently thin layers. Indeed, within the limit of a thin sample $h \ll \lambda$, the effective penetration length l can increase dramatically. The London length must be replaced by the Pearl length Λ [47]:

$$\Lambda(T, l) \approx \frac{\lambda^2(T, l)}{h}$$

Superconducting films of a few nanometers thickness are thus in the Pearl limit because λ is generally of the order of a few hundred nanometers. Specifically, for the samples studied below , the Pearl length Λ reaches several tens of microns, while the lateral dimensions of the systems are of the order of a few hundred nanometers. The limit $D \ll \Lambda$ is thus extremely well justified.

3.2.2 Vortex states in small superconductors

In type II superconductors, at thermodynamic equilibrium, vortices enter the sample beyond the first critical field H_{c1}. The number of vortices increases with the magnetic field until the second critical field $H_{c2} = \frac{\phi_0}{2\pi\mu_0\xi^2}$ where a normal state is reached within the sample because the vortex cores overlap. In 1963, St. James and de Gennes [50] showed that the superconducting state could exist beyond H_{c2} near an interface with

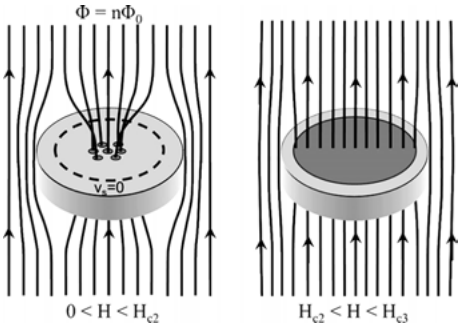

Fig. 3.3: Left: Vortices in a bulk type II superconductor with a diameter $D \gg \lambda$. For a low density of vortices there exists a region on the edge of the sample where the field is screened over a distance λ from the edge and from the vortices. In this region it is possible to find a contour (dashed line) over which the supercurrent velocity cancels. The flux of the magnetic field inside this contour is $n\Phi_0$, where n is the number of vortices within the contour. Right: a bulk superconductor in a magnetic field H such as $H_{c2} < H < H_{c3}$. In the inner sample vortices overlap and form a normal state region (in blue) while superconductivity is still present on the edge over a rim of thickness ξ (in gray).

an insulating medium to a third critical field $H_{c3} = 1,695H_{c2}$. This surface superconductivity extends over a thickness of the order of ξ at the edge of the sample as shown in Figure 3.3. Similar phenomena appear in confined superconductors, but the critical fields involved are different. In particular, the first critical field $\mu_0 H_{c1} = \frac{\phi_0}{4\pi\lambda^2} \ln(\lambda/\xi)$ clearly implies the penetration depth: if we neglect the logarithmic term we see that the first critical field is the one that generates a flux quantum in a disk of diameter 2λ. In a sample with diameter $D \ll \lambda$ such a critical field has hardly any meaning; the first critical field, that is to say the field at which the first vortex penetrates, will be directly dictated by the diameter of the sample rather than λ. The second critical field, meanwhile, will be difficult to define in samples of diameter $D \sim \xi$ because at this level there are no clear differences between bulk superconductivity and surface superconductivity. However the H_{c3} terminal field, where the entire sample becomes normal, remains well defined experimentally, its value will be modulated by the sample size and will greatly deviate from the values obtained in volume.

The generally widespread image of an isolated vortex in a superconductor is that of a tube of magnetic field carrying a flux quantum ϕ_0 (Figure 3.3). An isolated vortex acts like a current swirl around a normal core with supercurrents decreasing as $j \propto \frac{1}{r}\mathrm{Exp}(-r/\lambda)$ for $r \gg \xi$. This naive picture in terms of the flux bundle is causing much confusion in the interpretation of confinement phenomena in superconducting nanosystems. For a better understanding of the phenomena associated with confined vortices it is best to return to the most basic possible definition of a vortex. Quantum condensates, whether Bose–Einstein condensates of cold atoms or superfluid helium, admit all vortices when the condensates are put in rotation. In these neutral condensates, vortices are defined as singularities in the phase field of the order parameter. As

the wave function has to be single-valued, the circulation of the gradient of the phase around a vortex must be a multiple of 2π. In the case of an Abrikosov vortex the phase turns by 2π around the vortex core; we deduce that, very close to the core, the phase gradient is $|\nabla\varphi(\boldsymbol{r})| = 1/r$. This $1/r$ dependence indeed appears in the formula for the current flowing around the vortex in bulk samples $j \propto \frac{1}{r}\mathrm{Exp}(-r/\lambda)$, however there is an additional dependence $\mathrm{Exp}(-r/\lambda)$ which comes from the fact that the vortex currents generate a magnetic screening field which decays exponentially over a distance λ. These two contributions are better seen in the general expression for the current $\frac{1}{4m}\left|\left(\frac{\hbar}{i}\nabla - 2e\boldsymbol{A}(\boldsymbol{r})\right)\psi(\boldsymbol{r})\right|^2$ where the term $1/r$ comes from the phase gradient, while the screening term in $\mathrm{Exp}(-r/\lambda)$ is due to the magnetic field generated by the vortex currents and is expressed by the vector potential term. In confined superconductors with $D \ll \lambda$ diameter, it is clear that the exponential dependence will be negligible. This is simply due to the fact that the samples are not large enough for vortex currents to generate a magnetic flux equal to ϕ_0. Given the size of the samples for which confinement effects occur, we can consider that the circulating vortex currents do not alter the applied magnetic field, as seen in the Meissner phase (Figure 3.2). This lack of effective screening leads us to consider that the structure of vortices in strongly confined superconductors resembles that of vortices in neutral condensates, such as superfluid helium or Bose and Fermi condensates of cold atoms, which are associated with no flux quantum but instead with a singularity in the phase field [1, 62, 64].

3.2.3 Fluxoid

If we consider an isolated vortex in a superconducting disk of diameter $D \ll \lambda$ in the absence of an applied magnetic field (Figure 3.4d), as might be the case for a vortex pinned on a defect, we find an interesting situation which may seem disconcerting at first glance. Indeed, as the diameter of the sample is much lower than the penetration depth, the magnetic field generated by the vortex currents is clearly insufficient to generate a flux quantum, or the commonly accepted vision of a vortex as a quantized flux tube… To understand the essence of the problem we must now introduce the concept of fluxoid, which will make the usual association of a vortex to a flux quantum clearer. A good comprehension of this point is essential to understanding the mechanisms at work in nanosuperconductors.

The magnetic field flux Φ_S through a surface S is directly linked to the circulation of the vector potential on a contour δS:

$$\Phi_S = \iint_S \boldsymbol{B}\cdot \mathrm{d}^2\boldsymbol{S} = \iint_S [\nabla\times\boldsymbol{A}(\boldsymbol{r})]\cdot \mathrm{d}^2\boldsymbol{S} = \oint_{\partial S}\boldsymbol{A}(\boldsymbol{r})\cdot \mathrm{d}\boldsymbol{l}$$

Using the expression of the supercurrent which connects the superfluid velocity, the gradient of the phase and the vector potential: $\boldsymbol{j}(\boldsymbol{r}) = \frac{e}{\mathrm{m}}|\psi(\boldsymbol{r})|^2\left[\hbar\nabla\varphi(\boldsymbol{r}) - 2e\boldsymbol{A}(\boldsymbol{r})\right] = 2en_S\boldsymbol{v}_S$, there is a relationship between the flux of the magnetic field, the supercurrent

density vector and the phase gradient:

$$L = \frac{1}{2\pi}\oint_{\delta S} \nabla\varphi\,(\boldsymbol{r})\cdot d\boldsymbol{l} = \Phi_S/\Phi_0 - \frac{2m}{h}\oint_{\delta S} \boldsymbol{v}_S\,(\boldsymbol{r})\cdot d\boldsymbol{l}$$

This relationship defines the fluxoid L, also called the winding number of the phase. The phase should rotate by a multiple of 2π over the closed contour δS so as to keep the order parameter single-valued. Thus, the fluxoid L must necessarily be an integer. In the case of an isolated vortex in a bulk sample we can find a contour around which the current is canceled. This requires taking a contour passing at a distance much greater than λ of the vortex (Figure 3.3). Here, the current is canceled and the circulation of the superfluid velocity is zero. For an Abrikosov vortex, the phase rotates by 2π, i.e., the fluxoid is $L = 1$. We conclude that the magnetic field flux through the surface S surrounding the vortex is equal to a flux quantum: $\Phi_S = \Phi_0$. From this comes the usual image of the vortex as a magnetic tube carrying a flux quantum. If we now return to the case of a vortex confined in zero field in a sample of diameter $D \ll \lambda$ (Figure 3.4), we see immediately that the previous arguments no longer apply. This is because the circulation of the superfluid velocity does not vanish for any contour within the sample; in this case we cannot directly link the magnetic flux to the fluxoid. Thus, we can have an interesting case where the magnetic flux through the sample is almost zero ($D \ll \lambda$) while the fluxoid is $L = 1$. The fluxoid in this case comes from the circulation of the superfluid velocity $L \approx -\frac{2m}{h}\oint_{\delta S} \boldsymbol{v}_S\,(\boldsymbol{r})\cdot d\boldsymbol{l}$. For a hint of what is happening here, one can consider a circle of radius r for the δS circuit. It follows that $mv_s r = L\hbar$, which is none other than the quantization of angular momentum: a vortex of vorticity L confined in a nanodisk behaves like a 2D artificial atom with a wave function of angular momentum L. As we know from atomic physics the radial part of the wave function is directly related to the angular momentum; in the case of a vortex the consequence of this simple picture is that for a vortex or a giant vortex with $L = 1, 2, 3\ldots$, the radial dependence of the order parameter close to the core is r^L as will be shown later.

3.2.4 Zero-current line: Meissner versus vortex currents

As we can see, there is no need to have a quantum of flux in the system to have a vortex. However, in many situations, the notion of a flux quantum can be useful, even in the limit $D \ll \lambda$. This is particularly the case for a vortex in a cylinder in the presence of a magnetic field as described on Figure 3.4d. This figure describes the typical case where the Meissner currents induced by the magnetic field exceed the vortex currents at the edge of the cylinder. In a cylinder subjected to a perpendicular field B, the supercurrent velocity is given by $v_\theta = \frac{e}{2mr}(\phi_0 - \pi r^2 B)$. For $\pi r^2 B < \phi_0$, the current rotates in the clockwise direction as the vortex currents are dominant, while for $\pi r^2 B > \phi_0$ the current rotates in the opposite direction because the Meissner currents are dominant.

The velocity changes its sign when the flux $\pi r^2 B$ is becomes equal to the flux quantum ϕ_0. The explanation is simple, there is a zero-current line located at $r = \sqrt{\phi_0/\pi B}$ where Meissner currents and vortex currents compensate perfectly. Applying the fluxoid formula on the zero-current contour we find $L = \phi/\phi_0$. Thus, for a vortex with a quantum of fluxoid there is exactly one flux quantum within the zero-current line. By contrast, the total flux of the field through the island $\phi_{total} = \pi D^2 B$ will be greater than a flux quantum and has no reason to be quantified except for some accidental values of B.

3.2.5 Kinetic energy balance: Meissner state

The competition between Meissner currents and vortex currents plays an essential role in the energy balance of the vortex configurations. In superconductors with $D \ll \lambda$ the penetration of vortices aims primarily at minimizing the total kinetic energy of the currents. For simplicity consider a disk as shown in Figure 3.4. In the absence of the vortex, only Meissner screening currents circulate with the following dependence: $j(r) = -\frac{e^2}{m} n_s B r$. As $j \propto B$, the currents increase linearly with the applied magnetic field; it follows a quadratic increase in the total kinetic energy (Figures 3.4a and 3.5e). Beyond a certain field the kinetic energy could exceed the condensation energy and the Meissner state become less stable than the normal state. However, before this happens, when the field induces currents near the critical current, the superfluid density begins to collapse and the gap closes when the system reaches the normal state as shown in Figures 3.4b and 3.5a. It is clearly seen in Figure 3.5e, in the case $L = 0$, that the kinetic energy begins to grow quadratically before falling and tending to 0 when the superfluid density collapses. This evolution is clearly manifested on the condensation energy (see Figure 3.5f), which is directly related to the superfluid density. At low field the condensation energy is practically unaffected, the superfluid density is almost the same as in zero field, while in a strong field the condensation energy tends to 0 as the gap closes. The sample thus eventually reaches the normal state when the total energy of the superconducting state reaches that of the normal state $\Delta E = E_{\text{supra}} - E_{\text{normal}} = 0$ (case $L = 0$ in Figure 3.5g).

3.2.6 Kinetic energy balance: Vortex state

When the field is increased, rather than switching from Meissner to normal state the system can accept one or several vortices, as shown on Figure 3.5b–d. The vortex currents partially compensate the Meissner current so as to minimize the total kinetic energy. The more the field increases the more the system accepts vortices until finally the normal state is reached.

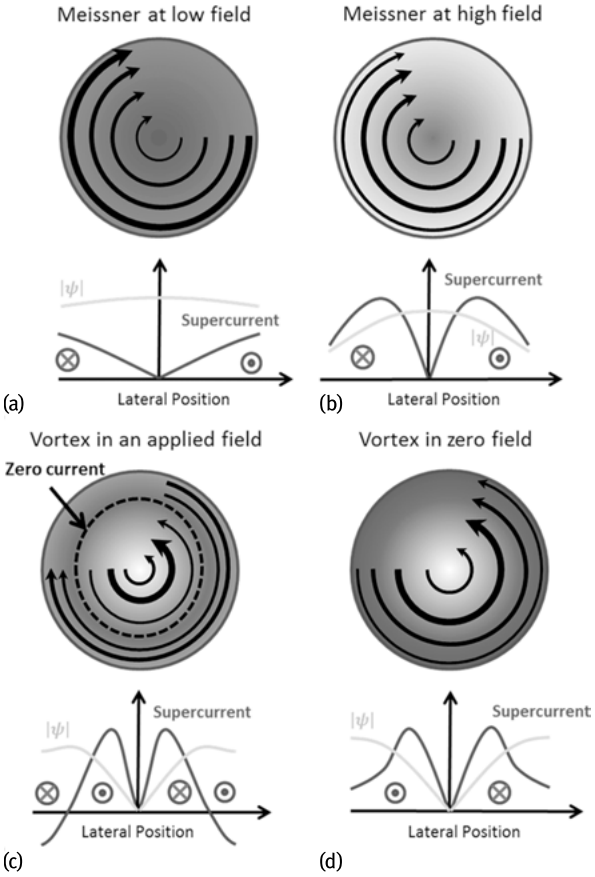

Fig. 3.4: (a) A disk in Meissner state in a small magnetic field. The current increases linearly with radius up to the edges, the order parameter is almost constant everywhere. (b) Meissner state close to the critical field: the currents flowing on the edge reach the critical velocity which reduces the order parameter and therefore the current density. (c) To minimize the effect of currents and remain superconducting beyond the critical field of the Meissner phase, the system accepts a vortex whose currents partially compensate Meissner currents. A line of zero current is formed in the disk; the flux of the magnetic field across the region bounded by the zero-current line is equal to a flux quantum. (d) A pinned vortex at zero field, no zero-current line present in the disk, the total magnetic flux through the sample is much less than a quantum of flux.

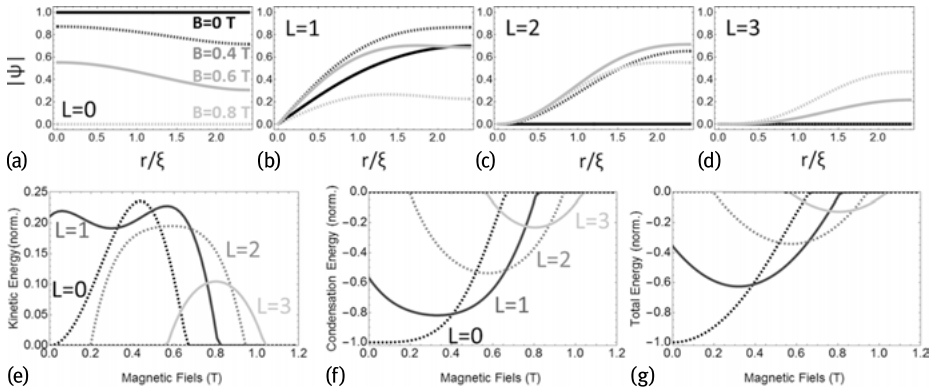

Fig. 3.5: (a–d) Modulus of the order parameter as a function of radius for a superconducting disk (R = 60 nm and ξ = 25 nm) as a function of the applied magnetic field for a vorticity $L = 0$ (a), $L = 1$ (b), $L = 2$ (c) and $L = 3$ (d). (e) Kinetic energy as a function of magnetic field to $L = 0$–3, the corresponding condensation energy is shown in (f), and the total free energy in (g).

As shown in Figure 3.5g, beyond a certain magnetic field, solutions with vortices become more stable than the Meissner state. The case of a single vortex is particularly enlightening for illustrating the delicate relationship between Meissner and vortex currents. But before analyzing the effect of currents, let us first recall the structure of an Abrikosov vortex core. Figure 3.5b shows that the order parameter linearly cancels in the vortex core: $|\psi(r)| \propto r$. The vanishing of the order parameter in the vortex core induces a loss of condensation energy. In a macroscopic sample the cost of a vortex core is $\mu = \pi\xi^2 \, h\epsilon_{\mathrm{cond}} = \pi\xi^2 \, hN(0)\,\Delta^2/2$, where h is the sample thickness and $\epsilon_{\mathrm{cond}} = N(0)\,\Delta^2/2$ is the condensation energy per volume unit. This shows that the core can be seen as a thick tube of height h and radius ξ in which the energy of condensation is zero. This image, though simple, is very useful in practice to estimate orders of magnitude.

To understand the mechanisms that govern the penetration of vortices in confined superconductors one must examine in detail the dependence of the kinetic energy and condensation energy as a function of applied magnetic field for different vortex configurations. For the case of a single vortex with $L = 1$, located at the sample center, the kinetic energy has two maxima and a local minimum, as shown in Figure 3.5e. This shape with two humps illustrates the mechanisms involved, as we now describe. The local minimum is due to the partial compensation between the vortex and Meissner currents (see Figure 3.4c). The maximum observed at a strong field is of the same origin as the peak observed for $L = 0$. There is an excess of Meissner current at the edge of the island that induces the destruction of the order parameter beyond a certain field, so there is an optimum between the increase of the superfluid velocity and the reduction of the order parameter. The destructive effect of the order parameter by Meissner currents can be seen on the profile of $|\psi|$ which decreases close to the edge (gray curve for

$B = 0.6$ T in Figure 3.5b). The first maximum is due to the vortex contribution and is also very well seen on the profile of $|\psi|$ near $r = 0$ (black curve $B = 0$ T in Figure 3.5b). It is clear that the order parameter near the vortex core is more strongly affected at zero field than at higher fields (dashed black curve $B = 0.4$ T and gray curve $B = 0.6$ T). This is because the vortex currents, not compensated by the Meissner currents, cause a marked decrease of the order parameter.

3.2.7 Kinetic energy balance: Giant vortex state

In the case $L = 2$ and $L = 3$ we see that no vortex state can be stabilized at zero-field. This comes from the intensity of the vortex currents: the superfluid velocity is given by $v_\theta = \frac{\hbar L}{2mr}$ in zero field, thus the kinetic energy of an isolated vortex increases quadratically with L (if $|\psi|$ constant). This kinetic energy goes hand in hand with a significant loss of condensation energy due to the fact that the vortex core radial dependence of the wave function changes dramatically with L : $|\psi(r)| \propto r^L$. The r^L dependence was predicted by D. St. James [52], it is clearly seen in Figure 3.5b–d.

In these Ginzburg–Landau calculations we looked for solutions with cylindrical symmetry, but for $L = 2$ and $L = 3$ we could find a solution in the form of two or three Abrikosov vortices with each $L = 1$ confined in the sample. This can be done by using more advanced calculations such as time-dependent Ginzburg–Landau equations. However, for the choice of parameters of Figure 3.5 we should still stabilize giant vortices. Understanding why a double vortex is more stable than two single vortices in this case is not easy. In the following we give some clues to understand what could lead several vortices to merge into a giant vortex. When a current flows in a superconductor the quasiparticle energy is modified by the Doppler effect: $E_{\boldsymbol{k}} = \sqrt{\epsilon_k^2 + \Delta^2} + \hbar \boldsymbol{k} \cdot \boldsymbol{v}_s$ [19], which provokes a widening of the gap. In practice this Doppler broadening effect is used for measuring the local superfluid velocity in tunneling experiments [7, 35]. As $|\boldsymbol{k}| \simeq k_F$, we see that if a quasiparticle of momentum $\boldsymbol{k}$ circulates in the opposite direction to the supercurrent its energy is decreased. Its energy can even become negative if the superfluid velocity v_s becomes greater than the critical value $v_d = \Delta / k_F$; this means that the Cooper pairs becomes energetically unfavorable beyond a certain critical depairing current. Note that at a distance ξ from a vortex core the superfluid velocity is given by $v_s = \frac{\hbar}{2m\xi} = \frac{\pi\Delta}{2k_F} = \frac{\pi}{2} v_d$. Thus, it is understandable that the gap starts to close at a distance of the order of ξ the vortex core because the supercurrent exceeds the critical velocity. If one now considers a giant vortex with $L > 1$, the superfluid velocity being proportional to L, $v_s(r) = \frac{\hbar L}{2mr}$, the critical velocity is reached at a distance of about $L\xi$ of a giant vortex. Thus, it is expected that these objects appear as normal tubes of radius $L\xi$ and area $L^2\pi\xi^2$ instead of $\pi\xi^2$ for an Abrikosov vortex. The cost in terms of condensation energy is in L^2 while the cost of L single vortices is just in L. A double vortex costs twice as much condensation energy as two single vortices, so multivortex configurations are more stable than giant vortices in large samples. How-

ever, in a strongly confined superconductor, the generation of two separated vortices has a significant additional kinetic energy cost. Having two separated vortices in a disk indeed means that the Meissner currents flowing near the edges will be strongly affected by the presence of these vortices. Some current lines will be trapped between the sample edge and the vortices, as if they were circulating in a constriction. The current conservation requires that the speed of the superfluid in the constriction becomes very high, causing a high cost (quadratic) in kinetic energy. It is as if the Meissner currents exerted a pressure on the vortices that forces them to go towards the center of the sample. These forces can become so strong that the vortices eventually merge into a giant vortex. In the following, we give some direct illustrations of this pressure effect by showing experiments where the Meissner currents provoke a strong confinement effect which, in some cases, will lead to the formation of giant vortex states.

3.3 STM/STS studies of vortices in nanosystems

3.3.1 Vortex core imaging by STM/STS

Vortices in superconductors are not only magnetic objects – flux bundles – but rather have a lot in common with the vortices observed in neutral condensate such as superfluid helium. It is therefore necessary to have a probe that allows investigating the vortex which doesn't rely directly on the magnetic field they produce. In fact, it is possible to do vortex imaging by probing the electronic structure in their cores. Caroli, Matricon and de Gennes indeed showed that the vortices behave like potential wells in which quasiparticles of energy located in the gap Δ are confined within a length scale of the order of the coherence length [11]. The first observation of the vortex cores was performed by Hess et al. in 1989, using scanning tunneling spectroscopy [29]. They showed that vortex cores in 2H-$NbSe_2$ are manifested by a peak in the local density of states (LDOS) around the Fermi level as predicted by Caroli, Matricon and de Gennes. In the case of superconductors in diffusive limit (mean free path l much shorter than ξ), the conductance peak in the vortex cores disappears and instead a simple normal state is recovered as shown by Renner et al. in 2H-$NbSe_2$ doped with tantalum [48]. The superconducting nanostructures elaborated for confinement studies are in the dirty limit (or diffusive limit) thus their vortex cores will be characterized by a normal state signature [15, 16, 43, 56].

There are several ways to address the problem of vortex confinement in nanoscale superconductors by scanning tunneling spectroscopy that can rely either on ex situ fabricated nanodevices or on in situ self-organized grown nanostructures. In all cases some important constraints have to be fulfilled. First, one must use a semiconductor substrate with a forbidden electronic band. Indeed, a metallic substrate in contact with the superconducting nanoislands would alter or even destroy superconductivity by the inverse proximity effect. However, tunneling microscopy requires conductive

substrates in the voltage range used for the tunneling spectroscopy, that is to say, a few millivolts. Unfortunately, at low temperature, the semiconductors are generally insulators for such voltage windows. The solution to this problem is to use substrates that are insulating in volume but which present a metallic surface state that allows for the evacuation of the current to external macroscopic electrodes.

3.3.2 STM studies on ex situ nanolithographed samples

Using nanostructured samples elaborated ex situ by electronic lithography is quite interesting if one wants to probe samples with regular shapes: disks, squares, triangles… with well-defined lateral size and thickness. Such a route is appropriate for checking some predictions like the coexistence of vortex and antivortex induced by confinement in particular geometries for instance [13, 63]. The problem with this method is that ex situ prepared samples generally have a very bad surface quality that strongly alters the quality of the STM/STS experiments. Most of the superconducting materials used for lithographed samples oxidize in air and thus one has to place a capping layer to protect the surface or to use particular materials that are less prone to surface contamination. Moreover, the samples prepared by nanolithography are generally not single crystalline and contain a lot of defects at the nanoscale which leads to some pinning of vortices. In many cases the vortex configurations are governed by the local pinning more than by confinement effects. However, progress with this lithography route is expected soon. For instance, quite recently a clever technique was developed that allows the imaging of vortex configurations in well-defined nanostructures fabricated ex situ with the help of electronic lithography [56]. The method relies on superconducting MoGe films that are deposited on a nanostructured SiO_2 sample. The nanostructures are defined by underlying Ge nanostructures on top of which the MoGe is deposited as can be seen in Figure 3.6a. With this method one obtains some MoGe squares on top of Ge mesas that are weakly coupled laterally to a conductive MoGe film that enables scanning tunneling experiments to be done. As the samples are prepared ex situ in a clean room their surface has to be protected from contamination by a thin Au film. As can be seen in Figure 3.6b the surface is quite rough, the topography exhibits a granularity that may behave as a pinning potential for vortices. However, nice regular vortex configurations with threefold and fourfold symmetry can be obtained that match quite well the theoretical predictions for vortex configurations in clean samples. A shell effect is also obtained when five vortices are confined in the square: four vortices form a square while the fifth one sits in the middle of the square. These results are quite encouraging and we may expect some rapid progress. However, Timmermans et al. [56] showed that there is still some weak pinning present due to the granular nature of the films. It seems quite unlikely that very clean samples could be obtained by the lithography route. For very clean samples another route has to be explored that relies on in situ growth of nanostructures as described in the following.

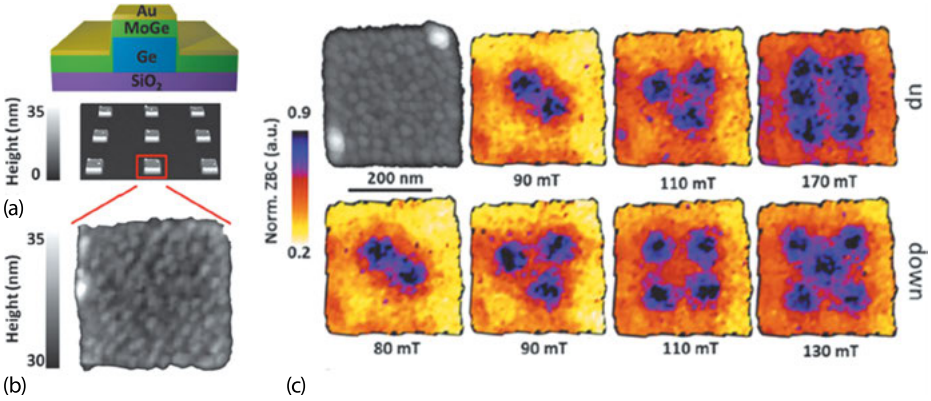

Fig. 3.6: Confinement of vortices in MoGe nanosquares. (a) Structure of the sample made of an MoGe film grown on a nanopatterned sample of Ge/SiO_2. The MoGe film is covered by gold in order to protect it from oxidation. (b) The topography of an MoGe square shows a rough surface with a granular structure. (c) Topography of a square and the corresponding conductance map at zero bias in different magnetic fields showing different configurations of vortices as a function of increasing magnetic field (up) and decreasing magnetic field (down) [56].

3.3.3 A model system for confinement studies: Pb/Si(111)

One of the most promising options for studying vortex confinement at nanoscale relies on the self-organized growth of nanostructures that generally allows for pure monocrystals exempt from defects and with an atomically clean surface. Among all the possibilities the system constituted by Pb nanoislands grown on Si(111) is certainly one of the best choices. Indeed, the Pb/Si(111) system has been extensively studied in surface science and a lot is known about the growth of Pb islands of various lateral size and thickness. Pb growth on Si (111) follows the Stranski–Krastanov mode, which results in the completion of a Pb wetting layer (1–2 monolayers) followed by the growth of nanoscale atomically flat Pb crystals [4, 30, 59]. For a deposition at room temperature without annealing, the wetting layer is amorphous and has all the characteristics of a bad metal with a low mean free path: it presents a very strong Altshuler–Aronov Coulomb correction of the density of states at the Fermi level [5, 54]. However, the wetting layer is sufficiently conductive to drain the charges injected by the STM, thereby allowing tunnel spectroscopy measurements to be made in good conditions.

The choice of Pb/Si(111) has been very successful for the study of confined vortices for several reasons. The first is that it is possible to obtain very flat and very pure monocrystals, several nanometers high and several hundred nanometers wide (see Figure 3.7). These dimensions are well suited to measurements by STM and are perfect to adjust the confinement effects. Indeed, by varying the growth conditions, we managed to develop different types of islands with adjustable thicknesses, widths and

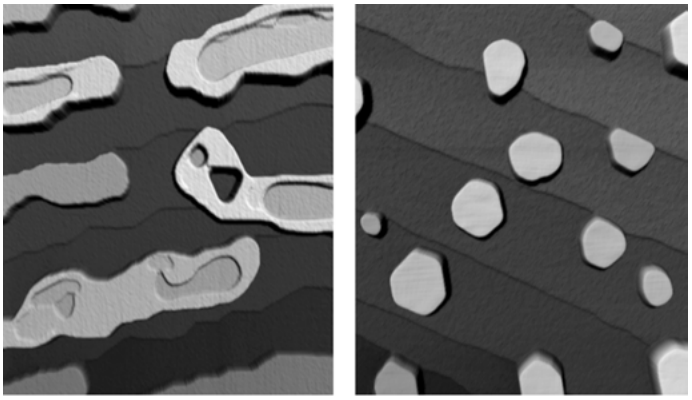

Fig. 3.7: Different types of islands of Pb/Si(111). (a) STM image $2.0 \times 2.0\ \mu m^2$ showing (111)-oriented 2D Pb islands with irregular edges and crowns obtained by depositing 5 monolayers of Pb at 290 K with a poorly outgassed Pb source. (b) STM image $1.2 \times 1.2\ \mu m^2$ showing flat and faceted islands obtained by depositing 3.5 monolayers at 260 K with a cleaner Pb source.

shapes. This allowed us to explore extreme confinement regimes, for example a regime where only one vortex can penetrate, or weak confinement regimes, where many vortices can penetrate. Figure 3.7 shows a number of very different forms of islands which we have grown by varying the growth conditions in a more or less controlled way, one of the crucial parameters is the purity of the lead source which evolves with the number of evaporations. As shown in Figure 3.7a, it is possible to obtain flat Pb islands oriented along the (111) direction that are elongated along the steps of the substrate and of irregular shape (little faceted edges, crowns, holes). This type of islands were obtained with a new source of lead or an almost empty one. The fact that the islands are only slightly faceted indicates that the diffusion of lead has slowed, which suggests the presence of impurities. With a Pb source that has been purified after many cycles of evaporation one obtains flat and well-facetted truncated-cuboctahedral islands oriented along (111) as shown in Figure 3.7b.

3.3.4 Ultimate confinement: The single vortex box

Using superconducting Pb islands with adjustable sizes grown in situ, low-temperature STM/STS experiments on the magnetic phase diagram of the nanoislands in different confinement regimes can be performed. To begin with we will tackle the most extreme case of all: an island that can accept at most one vortex (Figures 3.8 and 3.9) [16, 43]. The island shown in Figure 3.8a has a hexagonal shape with a diameter $D \approx 110\,\text{nm}$ and a thickness $h \approx 5.5\,\text{nm}$, and it has a slight hollow in the center. The coherence length in this island is $\xi_{\text{eff}} \approx 45\,\text{nm}$, corresponding to $D \approx 2,5\xi$, which should lead

to a strong vortex confinement. The effective London penetration depth is estimated to be $\lambda_{\text{eff}} \approx 150\,\text{nm}$ which is comparable to the diameter. But, as we have seen in the theoretical part, when the thickness is much smaller than λ, which is the case here, the penetration depth is given by the Pearl length $\Lambda = \lambda^2/h$. So the typical distance of screening of the magnetic field should be $\Lambda \approx 4000\,\text{nm}$, about 40 times the diameter! Under these conditions, the magnetic field will fully penetrate the sample, and we can consider, to a good approximation, that the magnetic field is equal to the applied field.

The phase diagram of this island was studied in various ways to obtain the most information possible about its response in a magnetic field. In the first method we mapped conductance by measuring the tunnel conductance at a temperature of 4.2 K (Figure 3.8b) at any point of the island for different applied magnetic fields. This yielded maps of the zero-bias conductance (ZBC) which reflect the supercurrent distribution in the sample in the Meissner phase (Figure 3.8d,e). As explained in the theoretical part the supercurrents produce a Doppler effect which causes a broadening of the BCS coherence peaks at the gap edge [7, 35]. At 4.2 K or $T \approx 0.65\,T_c$, because of the thermal broadening of 3.5 kT for the tunneling in S–I–N geometry, the Doppler effect is manifested by an increase in conductance at zero voltage while the density of states at the Fermi level remains zero, as long as the gapless regime is not achieved, as seen below.

Meissner state

The maps of Figure 3.8d,e were measured at 89 mT and 178 mT, in these fields no vortex is present in the island and the spatial variations in the conductance are only due to the depairing effect of Meissner currents. At a low field of 89 mT, the conductance is only weekly affected by the supercurrents, the blue color in the figure indicates a very low conductance similar to that in zero-field. When the field is doubled to 178 mT, the conductance map turns red at the edge of the island indicating that the gap is strongly affected by the Meissner currents. As shown in Figure 3.8c, the current is stronger at the edge and vanishes at the center. However, we see that at the center of the island the tunnel conductance is yellow-green, which means that the gap is already quite affected in the center of the island, while here the supercurrent is null. This effect, as P.G. de Gennes had anticipated, is related to the fact that the local density of states in a superconductor is sensitive to what is happening in a neighborhood of typical size ξ around the measuring point; the coherence length is the typical distance over which the order parameter and the superconducting state density vary. With the radius of the island $R \approx 1, 2\xi$, the center of the island is located at a distance of about ξ from the edge and therefore the local density of states at the center is strongly affected by the currents flowing on the edge. It is this nonlocal effect that limits the spatial resolution of the STM for imaging supercurrents. Despite this inherent limitation, it is clear that the conductance is higher at the edge than in the center, as expected because the

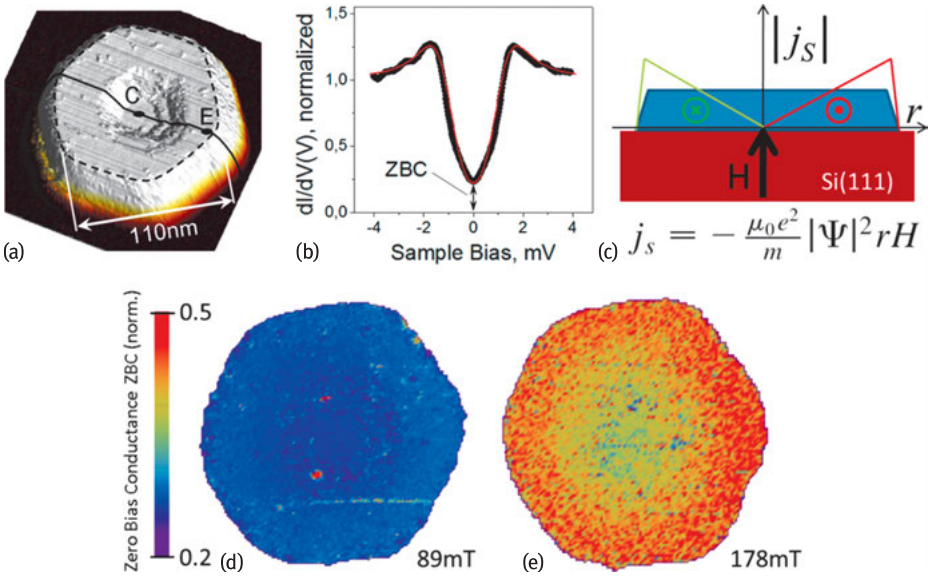

Fig. 3.8: (a) Image of a Pb island 110 nm in diameter and 5.5 nm thick at the edge. (b) Tunnel spectrum at zero field, measured at 4.2 K, showing the conductance at zero-bias ZBC which is used for plotting the conductance maps (d) and (e). (c) Profile of supercurrents in the Meissner phase. (d) Image of the ZBC at 89 mT, showing a slight increase in conductance along the island under the effect of supercurrents. Image (e) shows that at 178 mT the supercurrents flowing at the edge (in red) greatly affect the superconducting gap [16].

Meissner currents are stronger at the edge of the island. In normalized units (1.0 for the normal state) the conductance at zero voltage at the edge is about 0.5 (red) compared with 0.25 measured at zero-field. The zero-bias conductance (ZBC) is doubled due to the applied field and would quickly reach that of the normal state for a slightly higher field. As shown in Figure 3.9f, the evolution of the ZBC as a function of the field at the edge follows a quadratic dependence that recalls the kinetic energy of supercurrents (see Figures 3.5e–g) in the Meissner phase.

Single Vortex state

Beyond a certain magnetic field, the superfluid at the edge will exceed the critical velocity thus the order parameter will collapse and the sample will pass into the normal state or accept a vortex, if the sample is large enough. Here beyond $\mu_0 H_0 = 240\,\text{mT}$ the conductance in the center of the island is equal to that of the normal state (no gap), this means that above $H_0 = 240\,\text{mT}$ a vortex core is present (see Figure 3.9a,d,f). At field H_0, where the vortex penetrates the magnetic field flux through the island is $\phi = 1,22\phi_0$. One might naively think that the first vortex would penetrate as soon as a flux quantum passes through the sample, or even before because, by analogy

with the Little–Parks effect [38], one might think that the first vortex appears when $\phi = \phi_0/2$. In fact, the vortices tend to penetrate with a certain delay in nanosystems due to the presence of a vortex core which causes a loss of condensation energy of the order of $\pi\xi^2 \, h\Delta^2/2$, where h is the thickness. A vortex will thus penetrate if the loss of condensation energy is offset by the gain in kinetic energy, hence the delay.

The phase with one vortex shows a kind of re-entrant superconductivity which manifests itself in the form of a dip in the tunnel conductance at the edge of the island as a function of magnetic field (Figure 3.9e), with a minimum at $\mu_0 H_{\min} = 320\,\text{mT}$. This oscillation effect of the gap is also evident via the dependence of the ZBC as a function of the field at the center of the island (Figure 3.9f). This effect is related to the interference between the Meissner and vortex currents [16]. As we have seen in the theoretical part, in the presence of a vortex the superfluid velocity at a distance r from the center is given by $v_\theta = \frac{e}{2mr}(\phi_0 - \pi r^2 B)$, where the vortex contribution in $1/r$ partially compensates the Meissner currents which are proportional to r. When the vortex enters the sample, the magnetic field flux is $\phi = 1,22\phi_0$. As this is more than a flux quantum, there should be a zero-current line inside the sample through which passes just a flux quantum (see Figure 3.4c). Assuming a cylindrical geometry it is found that the zero-current line lies on a circle of diameter $D_0 = 100\,\text{nm}$, a little smaller than the diameter $D = 110\,\text{nm}$ of the island. Thus, the zero current line is very close to the edge. At a field $\mu_0 H_{\min} = 320\,\text{mT}$ (see Figure 3.9f) the zero-current line is on a circle of diameter $D_{\min} = 87\,\text{nm}$. As can be seen, increasing the magnetic field also increases the Meissner currents, pushing the zero-current line toward the center. At a given optimum field a compensation is achieved between the Meissner and vortices' currents, which results in the minimum conductance $H_{\min}$. Contrary to what would be observed for a Little–Parks ring [38], the minimum conductance obtained at $H_{\min}$ is significantly higher than the conductance at zero-field. This is due to the "proximity" effect of the vortex core which provokes a gapless superconductivity and also to the fact that the Meissner and vortex currents do not perfectly compensate.

Kinetic energy balance

Beyond the field $H_{\min}$, the Meissner currents dominate in the kinetic energy balance and the energy starts to grow quadratically (but offset by the conductance at $H_{\min}$) until the normal state is achieved at the terminal critical field $\mu_0 H_c = 460\,\text{mT}$. At H_c the total flux of the magnetic field through the island is $\phi = 2,32\phi_0$. One might think that for such a flux the system should have accepted a second vortex before transiting to the normal state, but it is not so. The delay between the number of vortices present in the island and the magnetic flux is in fact quite common. Intuitively, we can see that accepting a second vortex for $\phi = 2,32\phi_0$ would result in the formation of a zero-current line very close to the edge, meaning that the kinetic energy would be dominated by the vortex contribution. In this case the additional condensation energy cost due to the second vortex core will not be compensated by the gain in kinetic energy.

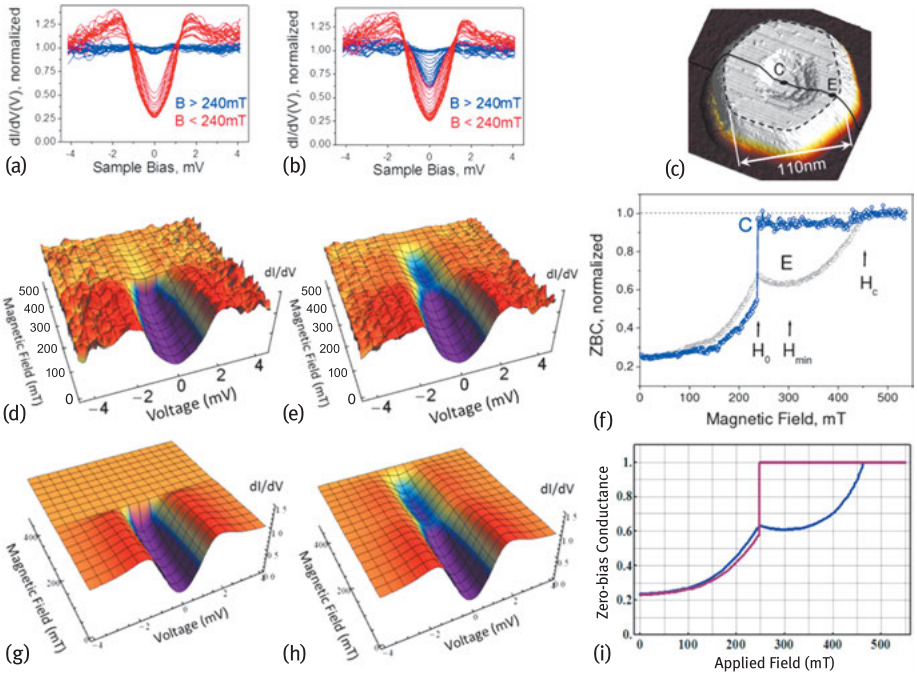

Fig. 3.9: (a) Tunneling spectra measured at the center of the island (point C on image c) depending on the applied field. The spectra are shown in red in the Meissner phase and blue after the penetration of a vortex. (b) Spectra measured at the edge of the island (point E on image c) depending on the applied field. (d) and (e) Evolution of the dI/dV tunneling spectra at the sample center (d) and edge (e) with the magnetic field. dI/dV scale extends from 0 to 1.5 as in (a) and (b). (f) Zero-voltage ZBC conductance depending on the field at the center (C) and the edge (E). The images g–h–i are calculated with Usadel equations and reproduce the observations d–e–f [16].

In a bulk superconductor the critical field is given by $\mu_0 H_{c2} = \frac{\phi_0}{2\pi\xi^2}$, for $\xi = 45$ nm the critical field would be $\mu_0 H_{c2} = 150$ mT, as compared to the 460 mT critical field of the island. This clearly illustrates that nanostructuration has the effect of multiplying the critical field by more than 3 for a given coherence length! However, as a bulk superconductor presents a surface superconductivity until $H_{c3} = 1,695 H_{c2}$, the third critical field in bulk would be $\mu_0 H_{c3} = 0.25$ T, which remains well below the critical field of the island. This amplification effect of the critical field is entirely consistent with what was expected as early as in 1965 by D. Saint James [51].

Usadel simulations

It is possible to reproduce all the effects described above by simulating the system with Usadel equations [57] in cylindrical geometry. Self-consistent calculations are shown in Figure 3.9g–i. The agreement with experiment is relatively conclusive and validates the physical description given above. The simulations were made by taking $T_c = 6.5$ K,

$\xi_{\mathrm{Bulk}} = 80\,\mathrm{nm}$, $\hbar\omega_D = 7.4\,\mathrm{meV}$, the only parameter left free being the mean free path. The numerical simulations lead to $l = 11\,\mathrm{nm}$, which corresponds to twice the thickness of the island. This relationship between the mean free path and the thickness was noticed by several teams working on Pb islands on Si(111) [15, 16, 42, 43, 45]. The fact that the mean free path is generally twice the thickness of the islands suggests that the interface between the island and the substrate is very diffusive. With such a mean free path the effective coherence length is $\xi = 45\,\mathrm{nm}$ as mentioned above, which corresponds to what was determined by studying vortex core profiles [16].

3.3.5 Confinement effect of supercurrents and surface superconductivity

After considering the limiting case of an island that cannot accept more than one vortex, we will consider the case of a larger island that can contain a dozen vortices. As a first approximation, in a sufficiently large island that accepts many vortices, the critical field should approach the third critical field $H_{c3} = 1.695\frac{\phi_0}{2\pi\mu_0\xi^2}$. The maximum number of vortices in an island of diameter D should roughly match the number of flux quantums through the sample at H_{c3}, hence the expected maximum number of vortices is $N_{\max} \approx \frac{\mu_0\pi D^2 H_{c3}}{4\phi_0} = 1.695\frac{D^2}{8\xi^2}$. The coherence length depends on the mean free path as $\xi = 0.85\sqrt{\xi_0 l}$. As experiments have shown that the mean free path is generally about twice the thickness h of the islands in Pb/Si(111), we get that the maximum number of vortices according to the diameter and the thickness is typically $N_{\max} \approx \frac{D^2}{8\xi_0 h}$. Thus, if one wants to reduce the confinement, one can increase the diameter, which is pretty obvious, or reduce the thickness, which is quite counterintuitive.

For an island 250 nm wide and 3 nm thick as the one shown in Figure 3.10, taking $\xi_0 = \xi_{\mathrm{Bulk}} T_{c\mathrm{Bulk}}/T_c = 113\,\mathrm{nm}$, and a mean free path $l = 2h = 6\,\mathrm{nm}$, we obtain an effective coherence length $\xi = 21\,\mathrm{nm}$. For these dimensions one should obtain a maximum number of vortices $N_{\max} = 11$. As seen in Figure 3.10, many vortices can enter, but it is difficult to say exactly how many, because beyond four it is too difficult to distinguish individual vortices due to vortex core overlap. However, it appears that at island edges, on a width of the order of ξ, a thin rim remains clearly superconducting (red-orange). This recalls the surface superconductivity predicted by Saint-James and de Gennes [50]. While inside the island the vortices induce a normal state, the edge is still superconducting. It is as if there was a vortex confinement effect forcing them to go to the center of the island. By comparing the conductance maps at 300 mT and 350 mT, we clearly see that when increasing the magnetic field a group of three vortices get much closer to the center of the island. This effect is again related to the competition between the vortex currents and Meissner currents: when increasing the field, the zero-current line which surrounds the three vortices is pushed inward, exerting a kind of compressive force on the vortex. It is precisely that pressure force induced by Meissner currents that can push so hard on the vortices that beyond a certain threshold several vortices will eventually merge. In the case of the island in Figure 3.10, when

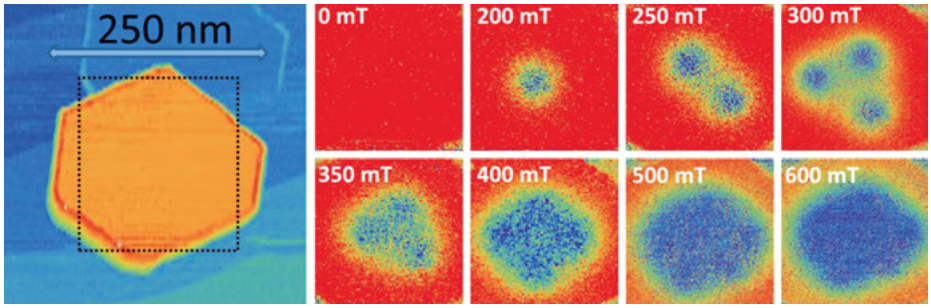

Fig. 3.10: Left: STM image of an island of a well-faceted Pb/Si(111). Right: zero-bias conductance maps as a function of the magnetic fields showing different vortex configurations; superconductivity appears in red, while the normal state appears in blue. The measured area is indicated by the dotted lines in the left image.

increasing the field beyond 400 mT, the system does not form a giant vortex because instead a fourth vortex penetrates. However, it is quite obvious that by choosing an island with a slightly smaller diameter, in which the confinement effects should be stronger, it should be possible to cause several vortices to merge into a giant vortex.

3.3.6 Imaging of giant vortex cores

First attempts to evidence giant vortex states

Several attempts to evidence giant vortex states were conducted either by magnetometry measurements [20, 24] or by multitunnel junction measurements [32]. These methods probe if some magnetic transitions take place that could be interpreted as the merger of several vortices into a giant vortex, but do not allow direct imaging. In particular Moshchalkov et al. predicted that upon field cooling certain small superconductors could show a paramagnetic response instead of a diamagnetic one, the so-called paramagnetic Meissner effect, attributable to the presence of a giant vortex [40]. Another approach based on magnetic imaging via the Bitter decoration method, showed the formation of dense clusters of vortices in samples subject to strong vortex pinning [26]. The authors interpreted these results as the possible existence of giant vortices, however a dense configuration of individual vortices is indistinguishable from a giant vortex because the spatial resolution of magnetic probes is limited to scales of the order of λ, which is insufficient to observe a phenomenon that happens at the scale of ξ in a type II superconductor. We will show in this section that the direct imaging of vortex cores by scanning tunneling microscopy permits us to reveal without any ambiguity the existence of giant vortices in strong type II nanoscale superconductors.

As noted previously the Meissner currents flowing at the edge of nanoislands cause a strong confinement effect on the vortices. According to Ginzburg–Landau calculations [8, 20, 22, 23, 40, 52, 53] it is expected that this pressure effect provokes the

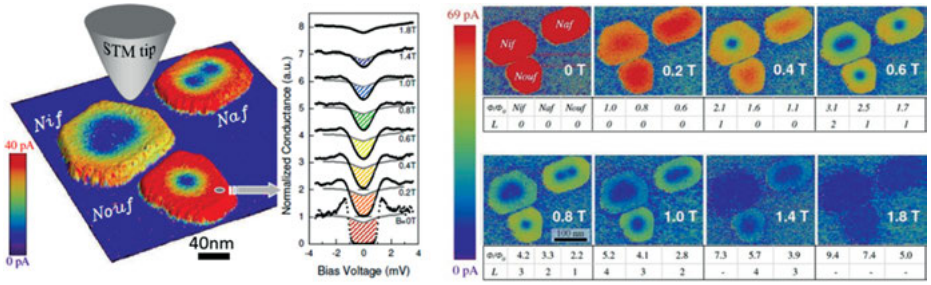

Fig. 3.11: Left: Combined STM topographic/spectroscopic image of Pb islands seven atomic layers thick and a few hundred nanometers in diameter in a field of 0.8 T. The color corresponds to the amount of states in the gap, as shown in the adjacent spectra. Under the effect of the magnetic field the superconductivity (in red) is gradually destroyed, vortices (blue) appear in the islands. The small island admits a single vortex, the medium island admits two vortices and the biggest one shows a large normal area in the center of the island which could be a dense cluster of several vortices. In the center, the tunnel conductance spectra show the density of states on the small island as a function of the applied magnetic field. Right panel: conductance maps as a function of the applied magnetic field from 0 T to 1.8 T [15].

merger of several vortices into a giant vortex (see Figure 3.1b). To observe this effect the lateral dimensions should be of the order of several times the size of a vortex core ($D \sim 5\xi$ in Figure 3.1b) so that the island can only accept a few vortices.

Pb/Si(111) strongly confined islands

In the experiment shown in Figure 3.11, three islands were measured together so as to optimize the chances of finding an ideal configuration, but also to compare different confinement regimes under the same experimental conditions. We will show that the smallest island of the three displays some giant vortex states with $L = 2$ and $L = 3$.

The principle of this experiment is shown in the left panel of Figure 3.11. Tunnel conductance spectra were measured for various magnetic fields for each point of the sample. As the experiment was conducted at 300 mK the spectroscopic resolution was excellent, but consequently it was no longer possible to image the effect of the Meissner currents in the zero-bias conductance maps because up to a field of 0.4 T the conductance remained zero at the Fermi level (see spectra in Figure 3.11). To image the effect of Meissner currents the spectroscopic maps were created by plotting the area in the gap (gapped area). The colored lines in the spectra give the correspondence between the color on the maps and the spectra. With this method it was possible to map very satisfactorily the distribution of Meissner currents as can be seen on the maps made at 0.2 T and 0.4 T (maps in Figure 3.11, right panel).

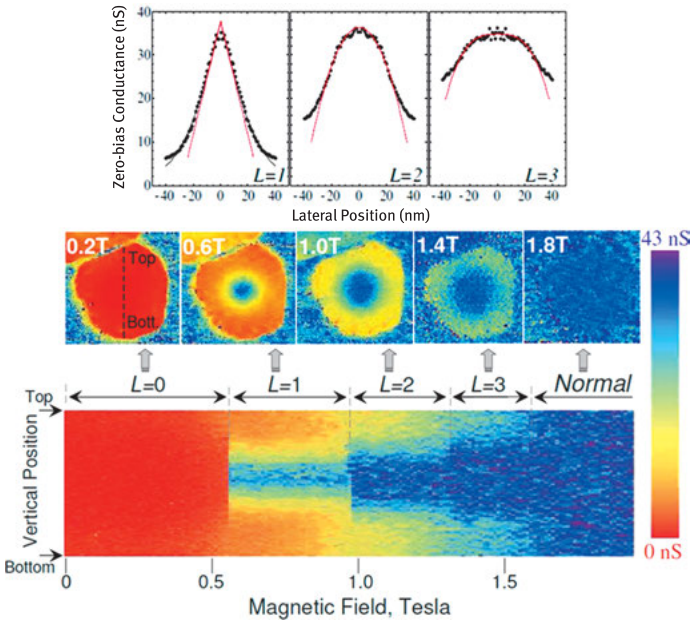

Fig. 3.12: Middle panel: conductance image of Nouf island of Figure 3.11 based on the field in the Meissner phase (0.2 T), the phase with one vortex (0.6 T), the phase with a giant $L = 2$ vortex (1.0 T), the phase with a giant $L = 3$ vortex (1.4 T) and the normal state at 1.8 T. Bottom panel: conductance as a function of the field along the section of the island shown in dashed lines. We distinguish conductance jumps that indicate the successive entry of three vortices. Top panel: a simple vortex profile $L = 1$, double giant vortex profile $L = 2$ and triple giant vortex profile $L = 3$, with an adjustment, shown in red, which is described in the text [15].

Meissner current depairing effect

In a field of 0.2 T the edge of the islands appears in a red-orange color which indicates the presence of strong Meissner currents. The largest of the islands, Nif, is the most affected, as expected given that the superfluid velocity increases with radius: $v_\theta \propto rB$. In a field of 0.4 T the Meissner currents in the large island would have exceeded the critical velocity if the island had not accepted a vortex. By contrast, the other two islands are still in the Meissner phase but it is clearly visible at the edge of the Naf island that the gap is almost closed (yellow-green) and therefore, for a slightly higher field such as 0.6 T, this island would be forced to accept a vortex in order to compensate the strong currents at the edge by counterpropagating vortex currents.

Strongly confined multivortex state

In a field of 0.6 T, the Nif island already admits two vortices, being wider than the others. These vortices are extremely close together, their distance is $d = 33$ nm, considering the estimated coherence length $\xi = 30$ nm it leads to $d = 1.1\xi$. Such an

intervortex distance is very small compared to the intervortex distance at the critical field in a bulk sample, $d_{Bulk} = 2.8\xi$. This clearly shows that the very high pressure induced by the Meissner currents pushes the vortices closer together than achievable distances in bulk samples. So one could hope that for higher magnetic fields, 0.8 T and 1.0 T, the Nif island would eventually accept a giant vortex. In the map of Figure 3.11 a large area in the normal state surrounded by a superconducting rim is observed, which could suggest a giant vortex, though a more detailed study described in [15] seems instead to point toward a dense vortex configuration forming a state close to surface superconductivity.

Giant vortex state

The brightest giant vortex signatures were actually obtained in the smallest island Nouf. On the detailed maps shown in Figure 3.12, for magnetic fields of 0.6 T, 1 T and 1.4 T, one can distinguish a round object in the center of the island, which can easily be attributed to a vortex. We see that this object appears to be wider when the field increases. To obtain more information on the structure of the vortex, we acquired spectra on a section through the island (black dotted line on the map at 0.2 T). The zero-voltage conductance as a function of field along this section is shown in the bottom of Figure 3.12. One can distinguish several regimes separated by discontinuities in the conductance, starting with the Meissner phase ($L = 0$), followed by the penetration of a single vortex ($L = 1$), then according to the conductance jump a second vortex penetrates a little before 1.0 T ($L = 2$) and finally a third vortex seems to penetrate at 1.3 T ($L = 3$). However, one can only distinguish a single vortex in the map at 1.0 T where one should see two vortices; and at 1.4 T where we expect three vortices a single round object appears in the map. To better understand what type of object it could be one can focus on a cut of the ZBC through these vortices as shown in the top curves of Figure 3.12. It appears that the vortex cuts for $L = 1$, $L = 2$ and $L = 3$ are very different. The first is entirely consistent with that of an Abrikosov vortex with a linear dependence of the conductance in the core (except in the center, $r \ll \xi$, where we find a parabolic profile). The case $L = 2$ is very different because it instead shows a parabolic shape and the case $L = 3$ is even more flared. These three conductance profiles were adjusted by the empirical curve $ZBC(r) \propto 1 - \left(\frac{r}{\sqrt{L}\xi_{\text{eff}}}\right)^L$ with a single fitting parameter for the three curves (red curves in Figure 3.12) [15]. The adjustment shows a r^L dependence of the conductance, which is in good agreement with the dependence r^L of the order parameter predicted by Saint-James in 1969 [52]. However, we must remain cautious as there is no direct link between the tunnel conductance and the order parameter. Further calculations with Usadel formalism should be conducted to confirm that the structures we observed are consistent with the theory for a giant vortex with vorticity $L = 2$ and $L = 3$.

3.4 Proximity Josephson vortices

3.4.1 Proximity effect

When a normal metal (N) and a superconductor (S) are put in contact their electronic properties near their interface are changed by the proximity effect. The spreading of Cooper pairs in the normal metal induces some superconducting correlations in it that manifest by an induced gap in the density of states and the ability to pass an electric current without dissipation through the normal metal. Very recently, the proximity effect has attracted attention from the surface physics community. It has indeed been demonstrated that in situ elaboration of superconducting nanostructures combined with tunneling microscopy/spectroscopy allows the proximity effect to be studied at a very high spatial resolution, providing new insight into this fundamental quantum phenomenon. In the following, after a few general explanations on the proximity effect, we will show some recent advances in this subject that have been established by the study of nanoscale superconducting-normal-superconducting Josephson junctions. We will show that with the help of the proximity effect it is possible to generate proximity Josephson vortices in a normal metal.

We will focus primarily on the proximity effect between a superconductor and a diffusive metal. One of the main signatures of the proximity effect is manifested by a change of the local density of states (LDOS) which can be directly measured at the nanoscale using scanning tunneling spectroscopy. The first tunneling measurements of the proximity effect begun in the 1960s using planar tunnel junctions formed by thin oxide barriers. These measures evidenced some spectral properties related to the proximity effect, but they could not probe the spatial aspects of the phenomenon. In the 1990s, Guéron et al. [27] were able to make nanotunnel junctions along a wire connected to a normal superconductor and to measure the local DOS at different distances from the SN interface; this was the first spatially resolved experimental study of the proximity effect. To improve the spatial resolution of tunneling experiments, different groups have used scanning tunneling microscopy/spectroscopy [21, 36, 41, 58, 60]. The first studies focused on ex situ fabricated nanostructures that posed serious technical problems for STM/STS, mainly due to surface contamination. Thus, the first spatially resolved STM experiments of the proximity effect [58] have been carried out on Nb-Au hybrid systems in order to profit from the chemical stability of Au in air. Here we will show how this experimental limitation was recently overcome by borrowing the methods of surface physics to develop hybrid superconducting nanostructures by self-organization under an ultrahigh vacuum. When developing hybrid structures in the same ultrahigh vacuum environment as the STM, the effect of surface pollution is greatly minimized. This helped researchers to probe the in situ proximity effect by STS experiments with high spatial and energy resolution [12, 33, 49, 54, 55]. In the following, we describe some recent experiments on hybrid SNS systems grown in situ which solved the longstanding problem of the internal structure of Josephson vortices.

3.4.2 Andreev reflection

In the modern view of the proximity effect, which emerged in the 1990s [34, 46], this phenomenon is closely linked to the notion of the Andreev reflection [6]. The Andreev reflection is a process in which an electron coming from N with an energy E (measured from the Fermi energy) is converted into a reflected hole of energy $-E$, thereby transferring a zero-energy Cooper pair to the electrode S. Alternatively, the Andreev reflection can be seen as the process by which a Cooper pair passes into N and becomes an electron pair, the two electrons being in states equivalent by time-reversal. This process governs the transfer of charge in an SN junction for energies below the superconducting gap of the S electrode, which are the relevant energies for the proximity effect. The two electronic states equivalent by time-reversal involved in the Andreev reflection diffuse into the normal metal and preserve their coherence over a distance $L_E = \sqrt{\hbar D_N/E}$ [28]. This length comes from the following process: because the difference in energy between the electron and hole states is $2E$, the relative amplitude of these two states becomes out-of-phase by a factor $\exp(-2iEt/\hbar)$ as the pair propagates through the normal metal, where t is the time elapsed since the pair left the superconductor. A phase shift of order 1 is obtained for $t \approx \hbar/E$. For such time the electrons diffuse over a distance of the order of $L_E = \sqrt{D_N t} = \sqrt{\hbar D_N/E}$, where D_N is the diffusion constant in the normal metal. Thus, $L_E = \sqrt{\hbar D_N/E}$ is the coherence length, i.e., the length over which the pair correlations decrease in the normal metal for the characteristic energy E. Therefore, the coherent propagation in N of two states with energy $|E| = \Delta$ will expand on a scale of characteristic length $\xi_N = \sqrt{\hbar D_N/\Delta}$, the normal coherence length. To conclude this discussion, we introduce another relevant energy scale in diffusive metals, namely the Thouless energy $E_{Th} = \hbar D_N/L^2$. To this end, we consider an SNS junction where the normal region has a length L. From our discussion above, it is clear that, at a given energy E, the superconducting correlations will extend through the wire as long as $L < L_E$, or equivalently, as long as $E < E_{Th}$. In other words, at a given distance L, only electrons having energies below the Thouless energy still present pair correlations.

3.4.3 Proximity effect in diffusive SNS junctions

In the normal part N of a diffusive SNS junction we expect to see some very peculiar features induced in the LDOS by the proximity effect. Figure 3.13a shows some calculations, with Usadel Theory, of the spatial variation of the LDOS in the case of an N bridge of length $L = 4\xi$ (where $\xi_N = \sqrt{\hbar D_N/\Delta}$), connected to the S electrodes by perfect interfaces at both ends. As shown in Figure 3.13a, the most notable feature is the appearance of a minigap $\Delta_g < \Delta$, which remains constant along the N region. This minigap gradually decreases as the length of the N bridge increases, as seen in Figure 3.13b. In the long junction limit, $L > \xi_N$ (or $E_{Th} < \Delta$), the minigap for fully

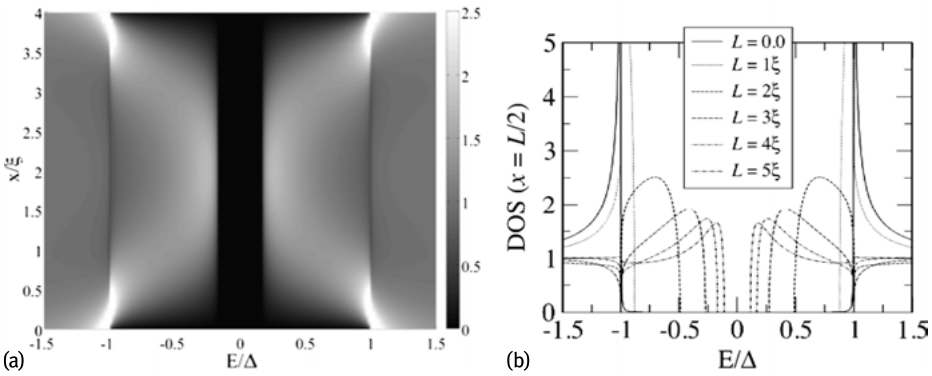

Fig. 3.13: (a) LDOS within the portion N of an SNS junction of a diffusive N bridge of length $L = 4\xi$ calculated in the framework of Usadel theory. Note the appearance of a constant width minigap through N. (b) LDOS in the middle of an SNS junction as a function of energy for different lengths of the wire N, $L = 0 - 5\xi$ [18].

transparent interfaces is simply given by $\Delta_g \approx 3,1E_{\mathrm{Th}}$. The appearance of a minigap in the junctions is a neat signature showing that some superconducting correlations propagate through the N bridge. As a consequence, the junction will be able to carry a supercurrent throughout the N part, and the SNS junctions will thus behave as a Josephson junction.

Using the system Pb/Si(111) it was possible to create local nanoscale Josephson junctions. They were obtained by adjusting the growth conditions so as to get islands sufficiently close to each other in order to form lateral SNS junctions with a normal part of width L comparable to a few ξ_{N}. As explained above the Pb/Si(111) system is characterized by the growth of flat Pb islands after the completion of a Pb wetting layer. The amorphous Pb wetting layer behaves as a weak link between two superconducting reservoirs formed by the adjacent islands. This geometry is similar to the SNS case discussed above. The geometry (Figure 3.14) allows experimental study of the minigap predicted in the N part of a S–N–S Josephson junction (Fig. 13a, b).

Figure 3.14 shows the case of two close superconducting Pb islands coupled together via the amorphous Pb wetting layer which is a strongly correlated diffusive metal. The SNS system is manifested by strong superconducting correlations induced in the N part as the zero-bias conductance map of Figure 3.14b shows. Clearly, a superconducting link forms between the two islands that appears as a zero-conductance region around the Fermi level (in brown). This zero conductance in the N part of the SNS junction is due to the presence of a minigap as shown in Figure 3.14c. The spatial dependency of the conductance spectra across the junction shows that in the N part there is a minigap of constant width of about 0.15 meV. By contrast, the superconducting islands located on either side of the N bridge present a much larger BCS gap of about 1.1 meV. This experiment thus provides a spatial representation of su-

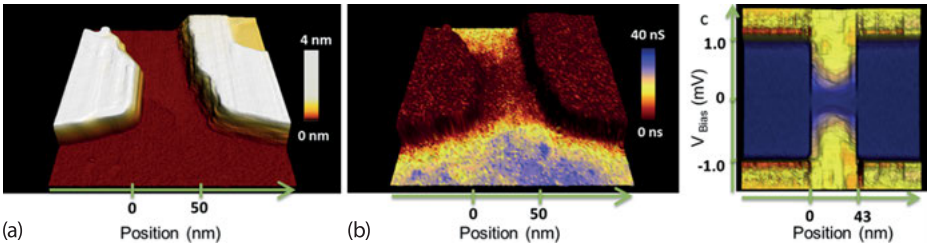

Fig. 3.14: (a) STM topography image showing two superconducting Pb islands (in white) separated by about 50 nm and connected via a normal amorphous Pb wetting layer (brown). (b) Zero-bias conductance image in color superposed on the topography in 3D showing the formation of a Josephson link (brown) in the SNS junction. (c) Cut of the LDOS through the SNS junction. A minigap of 0.15 meV appearing in blue is visible in the N region (0 to 43 nm), while the superconducting electrodes have a larger BCS gap of 1.1 meV.

perconducting correlations in a Josephson junction which is entirely consistent with what Usadel theory predicts for the SNS geometry in diffusive limit.

3.4.4 Josephson vortices in S–N–S junctions

As some superconducting correlations are induced in the N part of an SNS Josephson junction, one could expect that the metallic region will acquire some properties of superconductors. For instance, such an SNS junction can sustain supercurrents that flow through the N bridge. Another salient feature of superconductors is their response to a magnetic field and in particular the formation of Abrikosov vortices in type II superconductors. Then, a question that naturally arises is if the N part of an SNS junction will also accept vortices and if yes, what structure will they have? It is well known that the critical current of large Josephson junctions is modulated with the magnetic field and follows a Fraunhofer pattern [14, 61]. This modulation was interpreted as being attributable to the penetration of Josephson vortices into the junctions. In order to gain some insight into the nature of these vortices, Cuevas & Bergeret performed some calculations of the LDOS of an SNS junction in the presence of a magnetic field with the help of the quasiclassical Usadel formalism [9, 17]. On the basis of the Cuevas & Bergeret model, Figure 3.15a shows how the LDOS at the Fermi level varies spatially within an SNS junction for length $L = 4\xi$ and width $W = 4L$ and a magnetic flux $\phi = \mu_0 HLW = 2\phi_0$ through the N part. The first thing to notice is that, as expected, the LDOS is strongly modulated by the magnetic field. In particular, it seems that in the middle of the junction ($x = L/2$) there are areas where the superconducting proximity effect is completely suppressed (point C in Figure 3.15a). As demonstrated by Cuevas & Bergeret, this is the signature of the appearance of a Josephson vortex in the middle of the normal wire. They exhibit real vortex cores in which the superconducting correlations are suppressed, similarly to the suppression of the superconducting

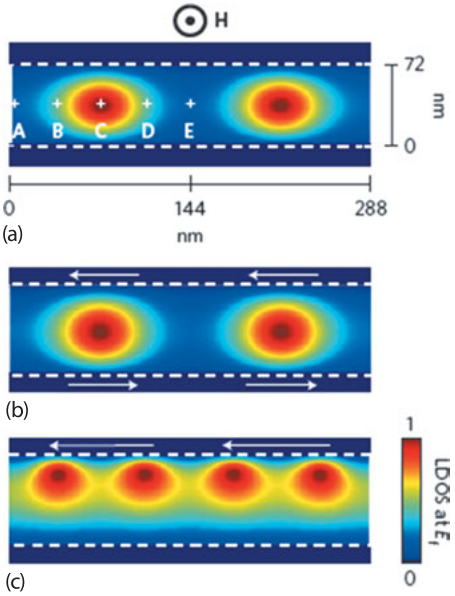

Fig. 3.15: Josephson vortex cores: local density of states and generating principle by currents. (a) LDOS at the Fermi level calculated by the Usadel approach for an SNS junction ($L = 72$ nm, $W = 288$ nm) subjected to a magnetic field of 200 mT. Note the appearance of two Josephson vortices. (b) Josephson vortices generated in an SNS junction by the presence of current in the S electrodes but in the absence of a magnetic field.(c) As previously, but with the current in a single superconducting electrode [49].

order parameter in Abrikosov vortex cores. These cores, where the LDOS is the one of normal state, are separated by regions where the minigap appears and where the spectrum is similar to the one observed in the absence of a magnetic field (point E in Figure 3.15a).

As shown in the next section, Josephson vortices are induced by a shear of the gauge invariant phase difference between the two superconducting electrodes. The magnetic field helps to generate such a shear, but it is not necessary. In fact, a supercurrent in the superconducting electrodes also generates a gradient of phase of the order parameter. If two currents flow in opposite directions, as shown in Figure 3.15b, some Josephson vortices will form in the junction under the shearing effect of the phase difference. If the current passes only through one of the two electrodes there are still some Josephson vortices in the junction, but they move close to the electrode where a supercurrent is flowing. Hence, it might be possible to generate proximity vortices without a magnetic field.

3.4.5 Imaging of Josephson proximity vortices

To verify the existence and ultimately determine the basic properties of the proximity Josephson vortices, we used a network of superconducting Pb islands connected by the Pb wetting layer (Figure 3.16) [49]. Each pair of islands forms an SNS junction; several of these SNS junctions are shown in Figure 3.16. These junctions were characterized by STM/STS in the absence and in the presence of a magnetic field. Figure 3.16a

shows a conductance map at zero bias in the absence of a magnetic field. It can be seen clearly that: (i) the Pb islands are superconductors (they have zero conductance at $V = 0\,\text{mV}$ due to the superconducting gap), (ii) the superconductivity is induced in the regions between the neighboring islands (lower conductance at zero voltage), and (iii) the remote area of the islands is in the normal state (the conductance is much higher and corresponds to the conductance of the wetting layer in the normal state).

Figure 3.16c shows conductance spectra acquired at three different locations (A, B and C) in the SNS junction named J1, see Figure 3.16a. As can be seen, the spectra are very similar and they all have a minigap, in agreement with the results discussed in the previous section. The situation changes when an external magnetic field is applied perpendicularly to the plane of the wetting layer. Figure 3.16b shows a zero-bias conductance of the sample acquired at 60 mT. This map shows the appearance of Abrikosov vortices in the Pb islands, but, more importantly, the tunnel conductance

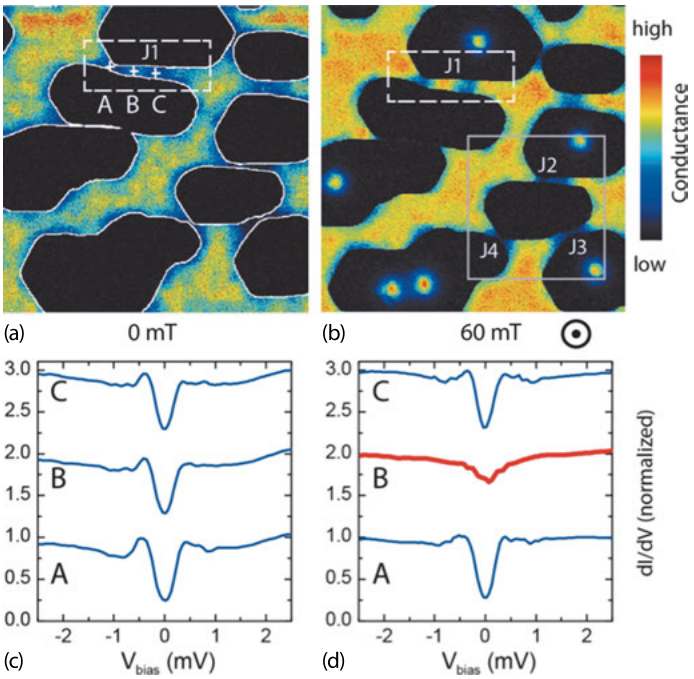

Fig. 3.16: Imaging of proximity Josephson vortices. (a) Zero-bias conductance image in zero field. The proximity effect appears as a blue halo around the superconducting lead islands. SNS Josephson junctions are formed in between the islands (dark blue). (b) In the presence of a 60 mT field, the proximity effect becomes spatially modulated in the SNS junctions, especially in the J1 junction which accepts a Josephson vortex in its center. (c) Conductance spectra showing a homogeneous minigap in three locations (A, B, C) of the junction J1 in zero field.(d) Spectra taken at the same location as in (c) in a field of 60 mT, the spectra measured in A and C are unchanged while spectrum B shows a LDOS representative of normal state, this is the signature of a proximity vortex core [49].

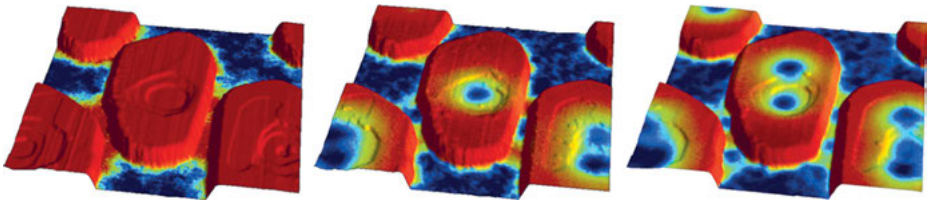

Fig. 3.17: Josephson vortex penetration at 0, 120 and 180 mT. Zero-bias conductance maps in color superimposed on 3D topography showing the superconducting gapped area in red and normal in dark blue. The measurement area corresponds to the gray rectangle in Figure 3.16. From left to right the field rises from 0 mT to 120 mT and 180 mT. We see a first vortex in the two junctions at 120 mT and then two vortices in each junction at 180 mT.

inside the N regions of the SNS junctions is spatially modulated along the transverse direction. This effect is particularly clear in the junction J1. We now analyze the conductance spectra acquired in the three areas A, B and C that are shown in Figure 3.16d. While spectra A and C show a proximity minigap very similar to the one acquired in zero magnetic field, spectrum B does not show any sign of a proximity effect; rather it reflects the spectrum of the wetting layer in the normal state. Note here that the normal state spectrum exhibits a small depletion at the Fermi level that has nothing to do with a minigap, it is in fact an Altshuler–Aronov zero-bias anomaly due to strong Coulombian correlations in the strongly diffusive wetting layer [5, 37]. The modulation of the minigap observed inside the SNS junctions is precisely the signature of the proximity Josephson vortices, as described in the previous section. The disappearance of the minigap is the signature of the presence of a vortex core there [49].

The proximity Josephson vortices can be seen more clearly in a zoom-in of the four islands forming the junctions J2, J3, J4 as indicated by the gray square in Figure 3.16b. To see the connection between the structure of the SNS junctions and the Josephson vortices we represented the conductance in color superimposed on the 3D topography as shown in Figure 3.17. This figure shows the junctions in three different magnetic fields: 0 T, 120 mT and 180 mT. The red color corresponds to zero conductance, i.e., a superconducting gap, while the blue-green color corresponds to a high conductance, that of the normal state. Josephson links appear clearly in zero field as zero conductance regions. In the presence of a magnetic field one can see that Abrikosov vortices appear in the islands and that Josephson vortices also appear in the junctions. The junctions J2 and J3 both admit a vortex at 120 mT, while by increasing the magnetic field at 180 mT both junctions admit two vortices. In Figure 3.17 we can see that the minigap disappeared in the center of junction J2 at 120 mT but it reappears at 180 mT. This behavior is expected due to the penetration of additional Josephson vortices in the junction.

3.4.6 Interpretation of the vortex structure

Shear of the phase difference

The structure of the Josephson vortex and the corresponding modulation of the local DOS are easy to understand within the limits of a wide junction ($W \gg L$). In this case, as we will show below, the role of the magnetic field is to change the superconducting phase difference ϕ between the two adjacent S electrodes. More importantly, we can show that, within that limit, the vortex cores located in the middle of the N junction form a linear array. The vortex cores appear at points such as $\phi = \pi, \pm 3\pi, \pm 5\pi$ where the minigap disappears due to an interference effect [36]. In addition, the minigap is fully recovered when ϕ is a multiple of 2π. Since the magnetic field induces a shear of the gauge invariant phase difference a series of Josephson vortices forms in the junction (see Figures 3.15 and 3.18).

Simulations with an extended Ginzburg–Landau Model

In order to show that a shearing effect of the phase difference causes Josephson vortices, we conducted phenomenological simulations, using a model based on the Ginzburg–Landau approach, to simulate the experimentally observed vortex configurations. The model reproduces the observations very accurately, as shown in Figures 3.19c and 3.20. Note that the model uses no adjustable parameter which makes the agreement between the model and the experiments quite robust. The purpose of these simulations is to illustrate that the Josephson vortices are induced by quantum interferences between the condensates of each superconducting island. Specifically, they show that the structure and position of the Josephson vortices are entirely determined by the phase portrait of the superconducting order parameter at the edges of the islands to which are added two constraints: minimizing the kinetic energy of supercurrents and current conservation (current flow into an island is zero).

The basic idea of the model is to calculate the Ginzburg–Landau order parameter in the Pb islands, taking into account their complex shapes and depletions to reproduce the observed Abrikosov vortex configurations. In these calculations the islands

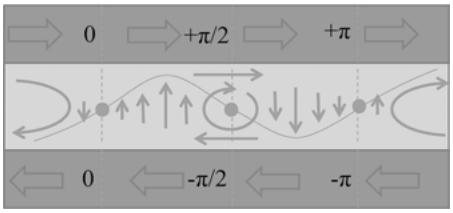

Fig. 3.18: Schematic diagram of a Josephson vortex. When the phase difference across the junction is $(2n + 1)\,\pi$ the minigap is destroyed by an interference effect. This gives rise to the formation of a vortex core in the center of the junction. The superconducting phase turns by 2π around the core; this is associated with a flow of supercurrent around the vortex.

are totally disjoint and uncoupled, but all calculations are done with the symmetrical gauge $\boldsymbol{A} = \frac{1}{2}\boldsymbol{B} \times \boldsymbol{r}$, where $\boldsymbol{r}$ is placed in the center of the image. This gives relatively complex phase portraits as seen in Figure 3.19b. In this model the observed Josephson vortex configurations can be reproduced by considering only interferences of superconducting evanescent waves taking into account an invariant phase difference $\varphi^* = \varphi(r_2) - \varphi(r_1) - \frac{2e}{\hbar}\int_{r_1}^{r_2} \boldsymbol{A}d\boldsymbol{l}$, where $\varphi(r_i)$ are the local phases of the order parameter on both sides of the island at positions r_i. The general idea is that for two opposite edges with φ^* equal to $0, \pm 2\pi, \pm 4\pi, \pm 6\pi, \ldots$ the superconducting correlations induced by nearby islands are in phase and result in constructive interference that result in a proximity minigap (see Figure 3.18). In contrast, in places where φ^* is equal to $\pm\pi, \pm 3\pi, \pm 5\pi, \ldots$ superconducting correlations interfere destructively, and the proximity gap is destroyed, which gives rise to Josephson vortex cores (Figure 3.18).

The implementation of the model is as follows. Once the phase portrait of each island is known, one considers evanescent waves over a distance ξ_N starting from each point $\boldsymbol{r}_i$ located on islands. These phenomenological evanescent waves represent the superconducting correlations in the proximity area. Each partial correlation contributes to the amplitude of the superconducting correlation map $\phi(\boldsymbol{r})$. All partial waves interfere in $\boldsymbol{r}$ according to their relative amplitude and gauge invariant phase difference:

$$\phi(\boldsymbol{r}) \propto \sum_i \int_{C_i} e^{-\frac{|\boldsymbol{r}-\boldsymbol{r}_i|}{2\xi}} e^{i\varphi^*(\boldsymbol{r},\boldsymbol{r}_i)} dl$$

where $\varphi^*(\boldsymbol{r}, \boldsymbol{r}_i) = \varphi(\boldsymbol{r}_i) + \frac{2e}{\hbar}\int_{\boldsymbol{r}_i}^{\boldsymbol{r}_i} \boldsymbol{A}d\boldsymbol{l}$. The phase $\varphi(r_i)$ is taken on the edge of the island i. The local magnitude of $\phi(\boldsymbol{r})$ correlations is thus given by the sum of the evanescent waves on C_i circuits around each island indexed by i. It should be noted that each phase portrait $\varphi(\boldsymbol{r}_i)$ is defined up to an arbitrary offset $\alpha_i : \varphi(\boldsymbol{r}_i) = \varphi_{GL}(\boldsymbol{r}_i) + \alpha_i$.

Since in this model the phase of each island edge is set to an arbitrary global phase, one has to determine (N – 1) phase differences for N islands. To make the model fully self-consistent, the phases were fixed so as to cancel the currents in-between the islands (Figure 3.19c, d) which generally gives two possibilities. To distinguish these two possibilities the model opts for the phase that minimizes the kinetic energy of supercurrents in the junction (Figure 3.19e). The comparison between this model without any adjustable parameter and the experiments is very good as can be seen in Figure 3.20.

Proximity versus Abrikosov vortices

Proximity Josephson vortices are not perfectly identical to Abrikosov vortices for several reasons. For example, Abrikosov vortex cores are generally round (when they do not overlap too much) and their radius is given by the coherence length ξ, while Josephson vortices may have shapes and sizes depending on the geometry of the junction. For a very long junction ($L \gg \xi$) Josephson vortices should be extremely

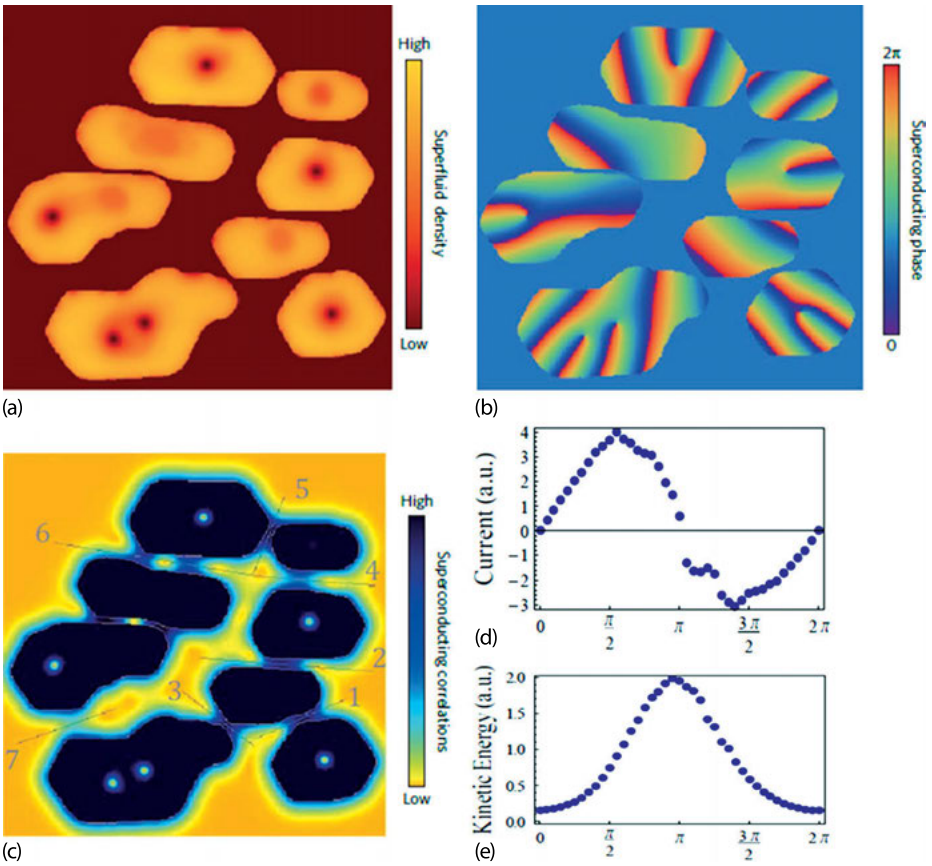

Fig. 3.19: Simulation method of Josephson vortex cores. (a) Module of Ginzburg–Landau order parameter of the islands in a 60 mT field. (b) Phase portrait of the order parameter. (c) Calculated superconducting correlations reproducing the experimental configuration of Figure 3.16b. (d) The current flow between two islands as a function of the global phase difference (for each junction the flow is calculated through the segments shown in (c)). (e) Kinetic energy of supercurrents as a function of the global phase difference [49].

elongated. Moreover, Josephson vortices form a line in the middle of junctions while Abrikosov vortices form a 2D network. Finally, in the cases we studied, the Ginzburg–Landau simulations clearly show that we can calculate the phase portrait for separate islands regardless of the back-effect of the junctions and reach an excellent agreement with the measurements. This means that superconducting correlations in the wetting layer do not influence the phase portrait in the islands, but only set the overall phase difference between the islands. Thus, the Josephson vortices are totally constrained by what happens in the S electrodes and do not seem able to exert a back-action on islands other than to adjust an overall phase difference; they are sort of passive objects.

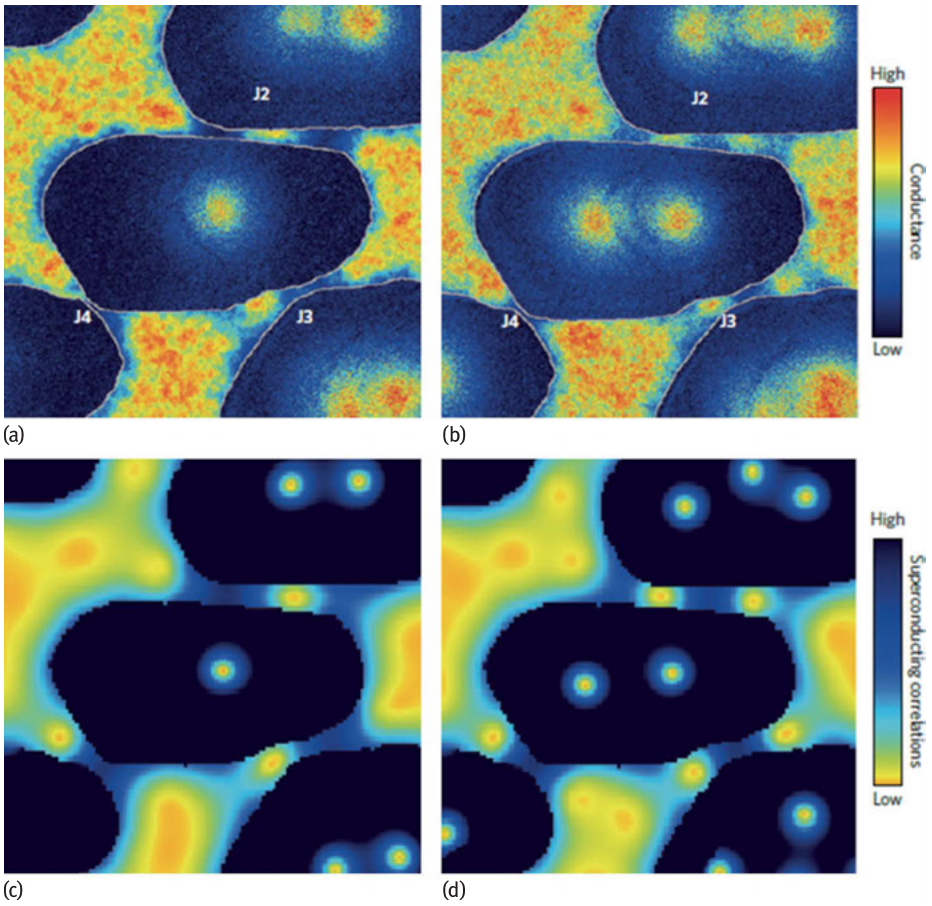

Fig. 3.20: (a) and (b): Conductance maps at the Fermi level at 120 mT and 180 mT showing the appearance of multiple Josephson vortices. The images in (c) and (d) are numerical simulations of the spatial variations of superconducting correlations; the Abrikosov and Josephson vortex configurations are calculated with the fully self-consistent model described in the text. A good general agreement is observed [49].

Finally, the Josephson vortices have many different properties from Abrikosov vortices making them unique quantum objects, not to mention the fact that they appear in a nonsuperconducting material!

3.5 Conclusion

In this chapter we explored different kinds of vortex confinement in nanoscale superconductors. We have shown that in the limit of samples with a lateral size much

shorter than the penetration depth the vortices could no longer be considered flux bundles but instead they have to be seen as a singularity in the phase field, as is the case for other superfluids such as superfluid helium or quantum condensates of cold atoms. In this limit, the vortex physics can be understood as a competition between the kinetic energy, which depends on both vortex and Meissner currents, and the loss of condensation energy associated with the formation of vortex cores. We explored a strong confinement regime where the coherence length, which gives the typical size of the vortex core, was comparable to the size of the system. In this limit, we found that the vortices are strongly confined by Meissner currents. We showed that in strongly confined systems, because of the pressure induced by Meissner currents, several vortices could merge to form a giant vortex state. In addition to this new type of vortex, we showed that a normal metal could also exhibit vortex cores due to the proximity effect. The proximity Josephson vortices observed inside SNS junctions are induced by a shear in the relative phase of the two superconducting electrodes. A magnetic field was used to generate the phase shear, but a supercurrent in the superconducting electrodes could also generate a phase gradient. Hence, it might be possible to generate proximity vortices without a magnetic field. This could be a good trick for elaborating nanoscale quantum-electronic devices based on vortex manipulation. For instance, proximity vortices induced in surface states of topological insulators should exhibit a Majorana zero energy bound state in their vortex core. It would then be possible to braid the Majorana vortex core states by applying some current in the nearby S electrodes and pave the way towards quantum computing.

Bibliography

[1] Abo-Schaeer JR, Raman C, Vogels JM, Ketterle W. Science 292:476, 2001.
[2] Abrikosov AA. J. Phys. Chem. Solids 2:199, 1957.
[3] Abrikosov AA. Sov. Phys. JETP 5:1174, 1957.
[4] Altfeder IB, Matveev KA, Chen DM. Phys. Rev. Lett. 78:2815, 1997.
[5] Altshuler BL, Aronov AG. In: Efros AL, Pollak M (eds). Electron-Electron Interactions in Disordered Systems. Elsevier Science Publisher B. V., Amsterdam, 1985.
[6] Andreev AF. Zh. Eksp. Theor. Fiz. 46:1823, 1964; [Sov. Phys. JETP 19:1228, 1964].
[7] Anthore A, Pothier H, Esteve D. Phys. Rev. Lett. 90:127001, 2003.
[8] Baelus B, Peeters F. Phys. Rev. B 65:104515, 2002.
[9] Bergeret FS, Cuevas JC. J. Low Temp. Phys. 153:304, 2008.
[10] Buisson O, Gandit P, Rammal R, Wang YY, Pannetier B. Phys. Lett. A 150:36, 1990.
[11] Caroli C, De Gennes PG, Matricon J. Phys. Lett. 9:307, 1964.
[12] Cherkez V, Cuevas JC, Brun C, Cren T, Menard G, Debontridder F, Stolyarov VS, Roditchev D. Phys. Rev. X 4:011033, 2014.
[13] Chibotaru LF et al. Phys. Rev. Lett. 86:1323, 2001.
[14] Clarke J. Proc. R. Soc. A 308:447, 1969.
[15] Cren T, Serrier-Garcia L, Debontridder F, Roditchev D. Phys. Rev. Lett. 107:097202, 2011.
[16] Cren T, Fokin D, Debontridder F, Roditchev D. Phys. Rev. Lett. 102:127005, 2009.

[17] Cuevas JC, Bergeret FS. Phys. Rev. Lett. 99:217002, 2007.
[18] Cuevas JC, Roditchev D, Cren T, Brun C. The Oxford Handbook of Small Superconductors, Chapter 4, Oxford University Press, 2016.
[19] de Gennes PG. Superconductivity of Metals and Alloys, Advanced Books Classics, Westview Press, 1999.
[20] Deo PS, Schweigert VA, Peeters FM, Geim AK. Phys. Rev. Lett. 79:4653, 1997.
[21] Escoffier W, Chapelier C, Hadacek N, Villegier JC. ; Phys. Rev. Lett. 93:217005, 2004.
[22] Fink HJ, Presson AG. Phys.Rev. 151:219, 1966.
[23] Fink HJ, Presson AG. Phys.Rev. 168:399, 1968.
[24] Geim AK, Grigorieva IV, Dubonos SV, Lok JGS, Maan JC, Filippov AE, Peeters FM. Nature 390:259, 1997.
[25] Ginzburg VL, Landau LD. Zh. Eksp. Teor. Fiz. 20:1064, 1950.
[26] Grigorieva IV, Escoffier W, Misko VR, Baelus BJ, Peeters FM, Vinnikov LY, Dubonos SV. Phys. Rev. Lett. 99:147003, 2007.
[27] Guéron S, Pothier H, Birge NO, Esteve D, Devoret MH. Phys. Rev. Lett. 77:3025, 1996.
[28] Guéron S. Quasiparticles in a Diffusive Conductor: Interaction and Pairing, PhD. Thesis, CEA-Saclay, 1997.
[29] Hess HF, Robinson RB, Dynes RC, Valles JM Jr, Waszczak JV. Phys. Rev. Lett. 62:214, 1989.
[30] Jalochowski M, Bauer E. Phys. Rev. B 38:5272, 1988.
[31] Josephson BD. Phys. Lett. 1:251, 1962.
[32] Kanda A, Baelus BJ, Peeters FM, Kadowaki K, Ootuka Y. Phys. Rev. Lett. 93:257002, 2004.
[33] Kim J, Chua V, Fiete AG, Nam H, MacDonald AH, Shih C-K. Nat. Phys. 8:464, 2012.
[34] Klapwijk TM. J. Supercond. 17:593, 2004.
[35] Kohen A, Proslier Th, Cren T, Noat Y, Sacks W, Berger H, Roditchev D. Phys. Rev. Lett. 97:027001, 2006.
[36] Le Sueur H, Joyez P, Pothier H, Urbina C, Esteve D. Phys. Rev. Lett. 100:197002, 2008.
[37] Lee PA, Ramakrishnan TV. Reviews of Modern Physics 57:287, 1985.
[38] Little WL, Parks RD. Phys. Rev. Lett. 9:9, 1962.
[39] Moshchalkov VV, Gielen L, Strunk C, Jonckheere R, Qiu X, Van Haesendonck C, Bruynseraede Y. Nature 373:319, 1995.
[40] Moshchalkov VV, Qiu XG, Bruyndoncx V. Phys. Rev. B 55:11793, 1997.
[41] Moussy N, Courtois H, Pannetier B. Europhys. Lett. 55:861, 2001.
[42] Ning YX, Song CL, Wang YL, Chen X, Jia JF, Xue QK, Ma XC. J. Phys.: Condens. Matter 22:065701, 2010.
[43] Nishio T et al. Phys. Rev. Lett. 101:167001, 2008.
[44] Nishio T, Chen Q, Gillijns W, De Keyser K, Vervaeke K, Moshchalkov VV. Phys. Rev. B 77:012502, 2008.
[45] Özer MM, Thompson JR, Weitering HH. Nat. Phys. 2:173, 2006.
[46] Pannetier B, Courtois H. J. Low Temp. Phys. 118:599, 2000.
[47] Pearl J. Appl. Phys. Lett. 5:65, 1964.
[48] Renner Ch, Kent AD, Niedermann Ph, Fischer Ø, Lévy F. Phys. Rev. Lett. 67:1650, 1991.
[49] Roditchev D, Brun C, Serrier-Garcia L, Cuevas JC, Loiola Bessa VH, Milosevic MV, Debontridder F, Stolyarov V, Cren T. Nature Physics 11:332, 2015.
[50] Saint-James D, De Gennes PG. Phys. Lett. 7:306 (1963)
[51] Saint-James D. Phys. Lett. 15:13, 1965.
[52] Saint-James D, Sarma G, Thomas EJ. Type two superconductivity, Pergamon Press, Oxford, 1969.
[53] Schweigert VA, Peeters FM, Singha Deo P. Phys. Rev. Lett. 81:2783, 1998.

[54] Serrier-Garcia L, Cuevas JC, Cren T, Brun C, Cherkez V, Debontridder F, Fokin D, Bergeret FS, Roditchev D. Phys. Rev. Lett. 110:157003, 2013.
[55] Stepniak A, Caminale M, Leon Vanegas MM, Oka H, Sander D, Kirschner J. AIP Advances 5:017125, 2015.
[56] Timmermans M, Serrier-Garcia L, Perini M, Van de Vondel J, Moshchalkov VV. Phys. Rev. B 93:054514, 2016.
[57] Usadel KD. Phys. Rev. Lett. 25:507, 1970.
[58] Vinet M, Chapelier C, Lefloch F. Phys. Rev. B 63:165420, 2001.
[59] Weitering HH, Heslinga DR, Hibma T. Phys. Rev. B 45:5991, 1992.
[60] Wolz M, Debuschewitz C, Belzig W, Scheer E. Phys. Rev. B 84:104516, 2011.
[61] Yang HC, Finnemore DK. Phys. Rev. B 30:1260, 1984.
[62] Yarmchuk EJ, Gordon MJV, Packard RE. Phys. Rev. Lett. 43:214, 1979.
[63] Zhang L-F et al. Phys. Rev. B 88:144501, 2013.
[64] Zwierlein MW, Abo-Shaeer JR, Schirotzek A, Schunck CH, Ketterle W. Nature 435:1047, 2005.